Validation and comparison of RANS propeller modeling methods for tip-mounted applications

Stokkermans, Tom C.A.; Van Arnhem, Nando; Sinnige, Tomas; Veldhuis, Leo L.M.

DOI
10.2514/6.2018-0542

Publication date
2018

Document Version
Final published version

Published in
AIAA Aerospace Sciences Meeting

AIAA SciTech Forum
8–12 January 2018, Kissimmee, Florida
2018 AIAA Aerospace Sciences Meeting

10.2514/6.2018-0542

Validation and Comparison of RANS Propeller Modeling Methods for Tip-Mounted Applications

Tom C. A. Stokkermans*, Nando van Arnhem*, Tomas Sinnige* and Leo L. M. Veldhuis†
Delft University of Technology, Delft, 2629 HS, the Netherlands

This paper examines the capability of a commercial RANS solver for the simulation of wingtip-mounted propellers. The applicability of actuator-disk and actuator-line models to reduce the cost of propeller modeling is investigated in its most accurate form, by extracting and applying propeller blade loading from full-blade simulations. The results obtained from all numerical simulations are validated based on measurement data from an in-house wind-tunnel experiment. An extensive grid dependency study is presented for the isolated propeller and the wing to distinguish discretization errors from model errors. It is concluded that RANS CFD with a simple one-equation turbulence model (Spalart–Allmaras) is capable of modeling the aerodynamic interactions for the wingtip-mounted propeller in tractor configuration, provided that numerical diffusion is accounted for by a grid dependency study or prevented by local grid refinement. The actuator-line model is fully able to replace propeller blade modeling in the simulation, and agreement with the full-blade simulations is found in time-accurate and time-average wing loading. The actuator-disk model further reduces the cost of the simulation by removing time dependency, at the cost of a small penalty in the accuracy of the time-averaged flowfield and lift distribution on the wing.

Nomenclature

B	=	Number of propeller blades
C_D	=	Drag coefficient
C_L	=	Lift coefficient
C_p	=	Pressure coefficient $C_p = (p - p_\infty)/q_\infty$
C_{p_t}	=	Total-pressure coefficient $C_{p_t} = (p_t - p_\infty)/q_\infty$
c_w	=	Wing chord
D_p	=	Propeller diameter
$\vec{F}$	=	Momentum vector per unit of time and volume
h_i	=	Average cell size of grid i
J	=	Advance ratio $J = V_\infty/(nD_p)$
$\vec{n}$, n	=	Unit normal vector, propeller rotational speed
p	=	Static pressure, observed order of accuracy
p_t	=	Total pressure
$\vec{Q}$, Q'	=	Torque vector, torque distribution
q	=	Dynamic pressure
R_p	=	Propeller radius
r	=	Radial coordinate in propeller reference frame
S	=	Energy per unit of time and volume
s_w	=	Wing semi-span
$\vec{T}$, T'	=	Thrust vector, thrust distribution
t_w	=	Wing thickness
U_s	=	Standard deviation of a fit based on observed order of convergence
U_ϕ	=	Estimated discretization uncertainty
u	=	x-velocity component
$\vec{V}$, V	=	Velocity vector, velocity magnitude
v	=	y-velocity component
w	=	z-velocity component
x	=	Axial coordinate
x'	=	Coordinate along chord of wing and flap
y	=	Lateral coordinate
y^+	=	Dimensionless wall distance
z	=	Vertical coordinate
α	=	Angle of attack
$\Delta E_{k_{rot}}$	=	Change in rotational kinetic energy
$\Delta E_{k_{tot}}$	=	Change in total kinetic energy
Δ_M	=	Maximum difference between solutions on different grids
Δx_c	=	Average cell size
δ_f	=	Flap deflection
δ_{RE}	=	Difference between estimated exact solution and solution on chosen grid, based on observed order of convergence
ε	=	Regularization function constant
η	=	Regularization function
Θ_b	=	Azimuthal location of blade b
θ	=	Azimuthal coordinate in propeller reference frame
ϕ_i	=	Numerical solution obtained using grid i
ω	=	Vorticity

Subscripts

p	=	Propeller
t	=	Tangential
x	=	Axial
θ	=	Azimuthal
∞	=	Freestream

Superscripts

$*$	=	Based on theoretical order of convergence

*Ph.D. Candidate, Flight Performance and Propulsion Section, Faculty of Aerospace Engineering, AIAA Member
†Full Professor, Head of Flight Performance and Propulsion Section, Faculty of Aerospace Engineering, AIAA Member

I. Introduction

Today's research on propellers is driven by their potential for reduced fuel consumption compared to turbofan propulsion. Not only the high propulsive efficiency of the propeller itself, but also its location on the airframe can enhance the overall efficiency of the aircraft. Wingtip-mounted propellers have been envisaged for their favorable interaction effects. For the tractor propeller variant, the interaction of the wing with the slipstream results in a reduction of the wing induced drag if the rotation direction of the propeller is opposite to that of the wingtip vortex [1, 2]. The pusher propeller variant experiences a reduction in shaft power due to the swirling vortex inflow from the wingtip in case the propeller rotates against the direction of the wingtip vortex [2–4]. Moreover, the modification of the wingtip vortex may reduce wing induced drag as well. Adverse aeroelastic effects due to the large weight of an engine at the tip of a wing and the large yaw moment arm of the thrust vector in case of a one-engine-inoperative condition, have prevented the application of wingtip mounted propellers up to now. The emergence of electric propulsion in aircraft allows almost penalty free downscaling of the propeller due to the scale independence of the electric motor [5]. This makes it possible to distribute of propulsion for instance through a hybrid-electric architecture and enables to scale down the wingtip-mounted propeller like proposed in the SCEPTOR concept [6]. Apart from the wingtip-mounted configuration, other concepts exist where the propeller is located on the tip of an aerodynamic surface with similar interactions, i.e. pylon-mounted propellers and propellers installed at the tip of the horizontal tailplane [7], see Fig. 1.

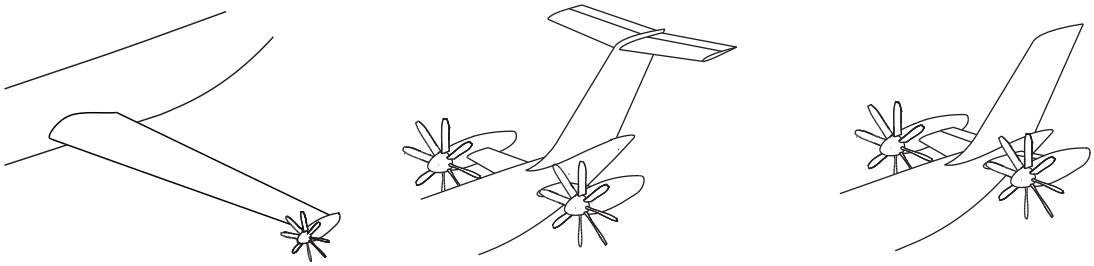

(a) Wingtip mounted (b) Pylon mounted (c) Horizontal tailplane mounted

Fig. 1 Three tip-mounted propeller concepts.

CFD simulations based on the RANS equations provide the right ingredients to model the interaction between a propeller slipstream and a wingtip vortex, because of the capability to capture both vortex interaction effects and viscous interaction effects. For the wingtip without propeller, research has shown that RANS CFD is capable of predicting the wingtip vortex with sufficient detail, although the large gradients in flow variables require locally dense grids [8]. For conventional wing-mounted tractor propellers, RANS CFD has proven to capture the transient propeller–wing interaction effects with adequate detail [9–11]. When the propeller is moved to the tip of the wing, the complexity of the flowfield increases due to the interaction of the propeller blade vortices and wingtip vortex, necessitating an evaluation of the accuracy of RANS simulations for this particular configuration.

Simulating a propeller interacting with an aerodynamic surface is computationally costly when resolving the propeller blades, especially in a preliminary design phase, where multiple concepts or design iterations need to be evaluated. Modeling of the propeller in a RANS simulation by sources of momentum and energy instead of resolving the propeller blades, has been shown to reduce the cost of the propeller–wing interaction problem [12]. These sources are added in a time-averaged sense with an actuator-disk (AD) model, but they can also be introduced in a time-accurate sense with an actuator-line (AL) model, as has been applied for wind turbines [13] and helicopter rotors [14]. In an actuator-line model, the propeller blades are replaced with distributions of momentum and energy sources along lines representing the blades. Next to the assessment of the accuracy of RANS simulations for wingtip-mounted propellers, it is especially interesting to evaluate the capability of these actuator models (AM). If proven to be sufficiently accurate, such modeling methods enable quicker design evaluations in propeller interaction studies.

The goal of the research presented in this paper is twofold. First, the capability of a commercial RANS solver for the simulation of wingtip-mounted propellers is investigated, by comparison of full-blade (FB) simulations with an in-house wind-tunnel experiment specifically designed for this purpose. Second, the applicability of actuator-disk and actuator-line models for this type of problem is studied by comparison with the full-blade simulations and the validation data from the wind-tunnel experiment. Actuator-disk or actuator-line models require the prescribed change in momentum and energy across the propeller. This paper focuses on the applicability of actuator models in their most accurate form: the propeller loading will be extracted from the full-blade propeller simulations and used as input. Future work will focus on the use of lower order tools to predict the blade loading based on the oncoming flow.

II. Validation Experiment Setup

The geometry used for the validation experiment dictated the geometry used for the simulations. Therefore, the setup of the validation experiment is summarized first. The full details of this experimental campaign are discussed by van Arnhem et al. [15]

A. Wind-Tunnel Facility and Models

The data set used for the validation of the RANS CFD analyses was measured in the Low-Turbulence Tunnel (LTT) at Delft University of Technology. This low-speed, closed-return wind tunnel features a test section with cross-section of 1.80 × 1.00 m with an installed reflection plane. At the selected freestream velocity of 40 m/s, the turbulence level is below 0.1%. Transition was forced on the reflection plane with a zig-zag transition strip.

A tip-mounted propeller configuration was installed in the wind tunnel by connecting a tractor propeller to the tip of a symmetrical wing model. A technical drawing of the propeller–wing configuration is provided in Fig. 2 and photographs of the model in the wind tunnel section are shown in Fig. 3. The propeller featured four straight blades and a diameter of 0.237 m, while the blade pitch angle was set to 23.9° at 75 % of the radius. The radial distributions of the blade chord and twist angle are provided in Sinnige et al. [16] Velocity and total-pressure data measured with the same propeller and nacelle in a sting-mounted configuration were taken from the same reference and used in the current paper to validate the simulations for the isolated propeller configuration.

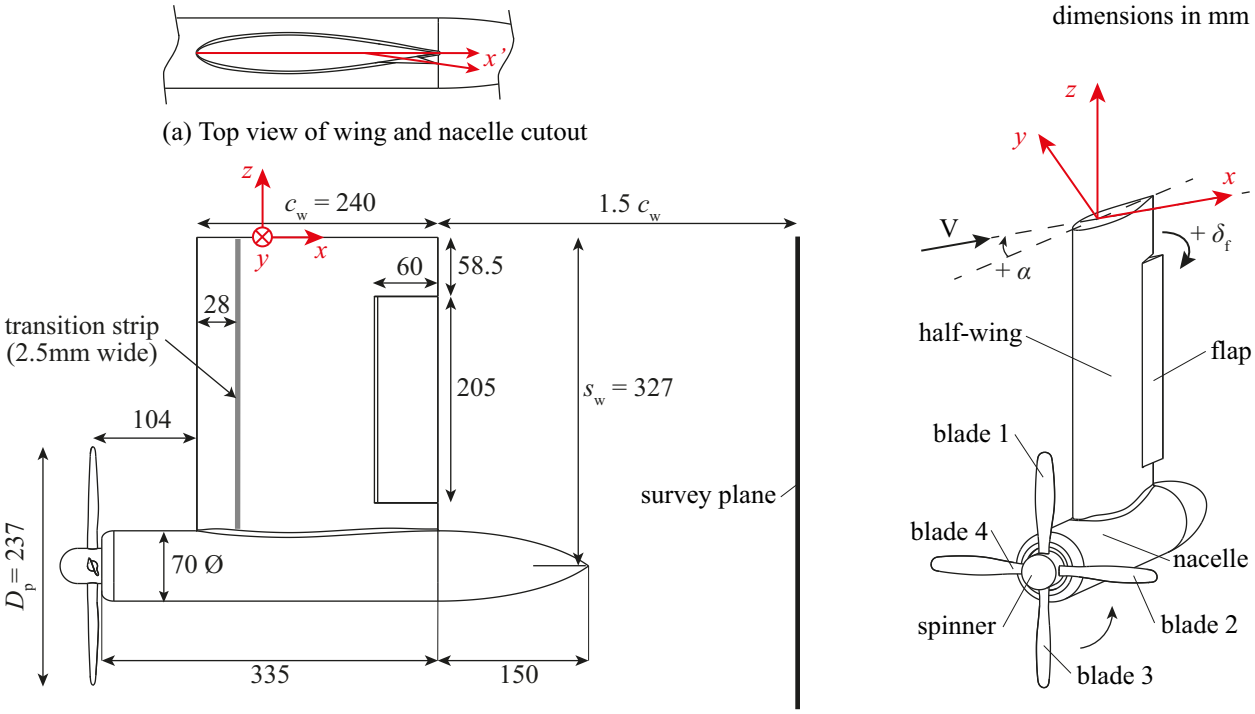

(a) Top view of wing and nacelle cutout

(b) Side view with survey plane location

(c) Isometric view

Fig. 2 Technical drawing of the test setup. The origin of the wind reference frame is located on the quarter chord of the wing root airfoil.

The nacelle was connected to a straight, symmetrical wing model with a chord length of 0.240 m, a semi-span of s_w = 0.327 m, and a NACA 64_2A015 profile with a round trailing edge of 0.0025t_w radius. The propeller–wing spacing was fixed to 43% of the propeller diameter, while boundary-layer transition at the wing was forced at 12% of the chord of the wing model using silicon carbide particles. A 25%-chord plain flap, integrated into the wing model, was used to simulate the effects of camber. The model was connected to a turntable integrated into the reflection plane, allowing for measurements at nonzero angle of attack.

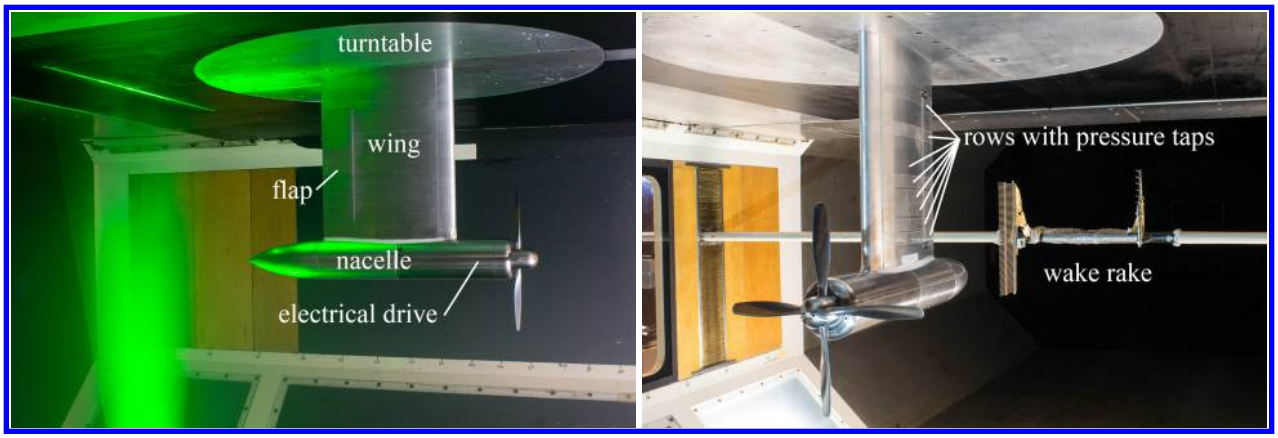

(a) Model geometry and PIV laser sheet at the survey plane (b) Wing pressure taps and wake rake

Fig. 3 Photographs illustrating the experimental setup and measurement techniques.

B. Measurement Techniques

The integral forces and moments generated by the propeller–wing configuration were acquired using an external six-component balance. The wing model contained a total of 408 pressure taps, providing local measurements of the pressure distribution at 8 spanwise locations as shown in Fig. 3 (b). Flowfield measurements were taken in the wake of the model using stereoscopic particle-image velocimetry (PIV). Three measurement planes were used at different z-locations, oriented perpendicularly to the flow at $1.5c_w$ downstream of the trailing edge of the wing model in the survey plane as sketched in Fig. 2. The measurement data obtained in the three planes were combined in postprocessing to obtain a complete description of the flowfield in the wake of the propeller–wing configuration. In Fig. 3 (a) the position of the survey plane with respect to the model is illustrated by the PIV laser sheet. The velocity data obtained from the PIV evaluations were complemented by pressure measurements using a wake rake, consisting of 50 total-pressure probes and 12 static-pressure probes. The wake rake was aligned such that the probes were positioned at the axial coordinate of the survey plane. The wake rake was traversed in the vertical and lateral directions, resulting in a spatial resolution of 2 mm for the total-pressure data and 4 mm for the static-pressure data. Figure 3 (b) illustrates the location of the wake rake in the test section.

C. Analyzed Test Cases

All measurements were taken at a freestream velocity of 40 m/s. For this paper only an angle of attack of 0° was considered for flap deflections of $\delta_f = +10°$ and $\delta_f = -10°$ with the blades removed and with the blades installed at an advance ratio of 0.8. The positive and negative flap deflection settings represent the cases for which the rotation direction of the wingtip-vortex is opposite or equal to that of the propeller slipstream swirl.

III. Computational Setup

A. Geometry

Simulations were performed for three different configurations:

Isolated propeller configuration The isolated propeller configuration contained the propeller, spinner and nacelle. Unlike the wind tunnel data from Sinnige et al. [16], no sting was present. Only a 90° wedge was modeled with one propeller blade. The geometry is the same as used in the wind tunnel model as shown in Fig. 2, but without the wing. The coordinate system for this configuration is located in the propeller plane with the x-axis through the rotation axis in downstream direction as presented in Fig. 4 (a).

Wing configuration The wing configuration consists of all the components shown in Fig. 2 except the blades. The transition strip was not modeled. The gaps around the flap that were present in the experiment were also incorporated in the numerical model: A gap was present along the front of the flap with a width of $0.027t_w$ perpendicular to the surface. A gap of the same width was implemented along the inboard flap edge. In the

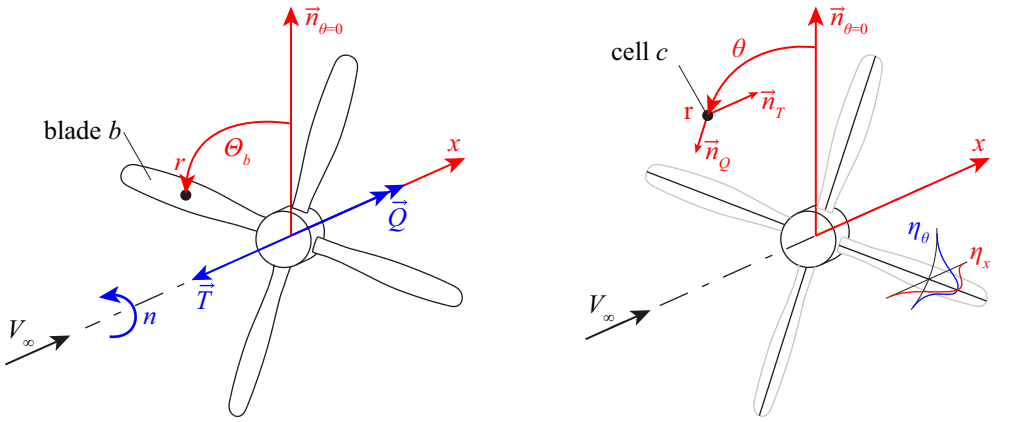

(a) Propeller reference frame definition (b) Actuator line and disk definitions

Fig. 4 Propeller reference frame definition including actuator model variables.

experiment, the outboard flap edge was flush with the wing and thus no gap was modeled there other than the gap arising from a flap deflection.

Propeller–wing configuration The propeller–wing configuration contained all components drawn in Fig. 2. The propeller was present for the full-blade representation of the propeller, while for actuator-disk and actuator-line representations of the propeller, a spinner without blades was used like in the wing configuration.

B. Propeller Modeling Methods

1. Full-Blade Model

The full-blade model contained the propeller blades on which the boundary layer was resolved including the viscous sublayer. Propeller motion was achieved by mesh rotation with sliding mesh interfaces between the stationary and rotating grid.

2. Actuator-Line Model

In the actuator-line model, the propeller blades were replaced with distributions of momentum sources and energy sources along lines representing the blades. See Fig. 4 (a) for the definition of a propeller reference frame located in the propeller plane with n the rotational speed and $\vec{T}$ and $\vec{Q}$ the thrust and torque vector respectively. Let $T'(r,\Theta_b)$ and $Q'(r,\Theta_b)$ be the radial thrust and torque distributions per unit of length acting along blade b with Θ_b the azimuthal location of blade b. For cell c in Fig. 4 (b), the momentum source term vector $\vec{F}(x,r,\theta)$ and energy source term $S(x,r,\theta)$ per unit of time and volume can be written as:

$$\vec{F}(x,r,\theta) = \eta_x\eta_\theta\left(T'\vec{n}_T + \frac{Q'}{r}\vec{n}_Q\right) \qquad S(x,r,\theta) = \eta_x\eta_\theta\vec{F}\cdot\vec{V} \tag{1}$$

where $\vec{n}_T$ is a unit vector opposing the thrust direction and $\vec{n}_Q(\theta)$ a unit vector opposing the local torque direction. The energy source term is equal to the work done on the fluid per unit of time and volume. The terms η_x and η_θ are regularization functions to smoothly distribute the source terms in the volume in axial and azimuthal direction to avoid singular behavior. A one-dimensional Gaussian kernel was chosen for each of them, based on the work of Sørensen et al. [17], in which a three-dimensional Gaussian kernel was succesfully used for an actuator-disk application. In the radial direction no regularization function is required, since the thrust and torque distributions are prescribed per unit of radial length. The regularization functions in axial and azimuthal direction are defined as:

$$\eta_x(x) = \frac{1}{\varepsilon\sqrt{\pi}}e^{-\left(\frac{|x|}{\varepsilon}\right)^2} \qquad \eta_\theta(r,\theta) = \sum_{b=1}^{B}\frac{1}{\varepsilon\sqrt{\pi}}e^{-\left(\frac{|\theta-\Theta_b|r}{\varepsilon}\right)^2} \tag{2}$$

where Θ_b is the azimuthal location of blade b of the total of B blades and ε is a constant to adjust the strength of the regularization functions. For each of the cells in the domain, the actuator-line model calculates the x, r and θ location

in the propeller reference frame. By updating Θ_b at each timestep and updating the azimuthal regularization function for each cell, actuator-line movement is simulated. The regularization constant ε was kept equal to the local cell size as recommended by Sørensen et al. [17] To achieve the goal of the paper, the actuator-line model was tested in its most accurate form: by extracting and applying blade loading from the full-blade propeller simulations of the same configuration.

3. Actuator-Disk Model

Instead of representing the blades by lines, in the actuator-disk model their averaged effect on the propeller disk was modeled, taking into account radial and azimuthal variations in loading. While the actuator-line model is inherently time-dependent, a simulation with the actuator-disk model can be solved as a steady problem. The source terms are the same as in the actuator-line model, except the azimuthal regularization function $\eta_\theta(r,\theta)$, which is replaced by:

$$\eta_\theta(r) = \frac{B}{2\pi r} \tag{3}$$

C. CFD Solver Setup

The RANS equations for compressible flow were solved 2nd order accurate using ANSYS® Fluent 16.0 [18], a commercial, unstructured, finite volume, cell-centered solver. For all simulations involving the full-blade model and actuator-line model, time-dependent solutions were found by a 2nd order backward Euler scheme with a time step equivalent to 2° of propeller rotation. Discretization of the advection term was done with an upwind scheme using the Barth–Jesperson boundedness principle [19]. For the equation of state, an ideal gas was assumed and Sutherland's law was used to predict the corresponding dynamic viscosity. Standard sea-level atmospheric conditions were used for the freestream flow, which was close to the experimental conditions (time-averaged).

The turbulence model was selected based on the findings of Kim and Rhee [8], who tested several turbulence models to simulate the wingtip vortex of an isolated wing. The eddy viscosity model in their research that best agreed with experimental data in terms of static pressure and axial velocity in the wingtip-vortex core was the Spalart–Allmaras (SA) one-equation model [20] with modification proposed by Dacles-Mariani et al. [21] to prevent build-up of turbulence viscosity in vortex cores. Therefore, this model was selected for the current research. The two-equation eddy viscosity $k-\omega$ model with shear stress transport correction [22] ($k-\omega$ SST) is often used for propeller simulations [23–26] and was therefore considered as well, although this model agreed poorly in terms of static pressure and axial velocity in the wingtip-vortex core in the research of Kim and Rhee [8]. In the current paper, a comparison is presented between these two turbulence models for the isolated propeller and wing configurations. Values for the inlet turbulence quantities were based on the recommendations by Spalart and Rumsey [27], which resulted in an eddy viscosity ratio of 0.21044 for the SA model and turbulence kinetic energy of 0.0016 J/kg and turbulence dissipation rate of 833 1/s for the $k-\omega$ SST model using the wing chord as the reference length. In order to fully resolve the boundary layer, the y^+ value on the no slip walls of the model was less than one.

D. Domain and Boundary Conditions

1. Isolated Propeller Configuration

A sketch of the domain including boundary conditions and dimensions used for the isolated propeller configuration is shown in Fig. 5. Since the wake of a propeller with axisymmetric nacelle is cyclic with the number of the blades, to reduce the cost of the problem only a single blade was modeled with periodic boundary conditions in a 90° wedge domain. This implies that the simulations were not performed in the wind-tunnel domain, as was done for the other models considered. The outer dimensions of the domain were chosen to be sufficiently large with respect to the propeller radius in order to minimize the influence of the boundary conditions on the flow properties near the propeller. At the domain inlet, a total-pressure jump with respect to the undisturbed static pressure was set to reach the freestream velocity of 40 m/s. Furthermore, the undisturbed total temperature was specified. At the domain outlet, the static pressure was prescribed to be equal to the undisturbed static pressure, averaged over the outlet surface. On the top of the domain, a Riemann-invariant pressure farfield condition was specified with a Mach number, static pressure and static temperature complying with the inlet conditions. The propeller blade, spinner and nacelle were modeled as no-slip walls. Due to geometrical overlap, the front part of the nacelle was in the propeller domain and was modeled

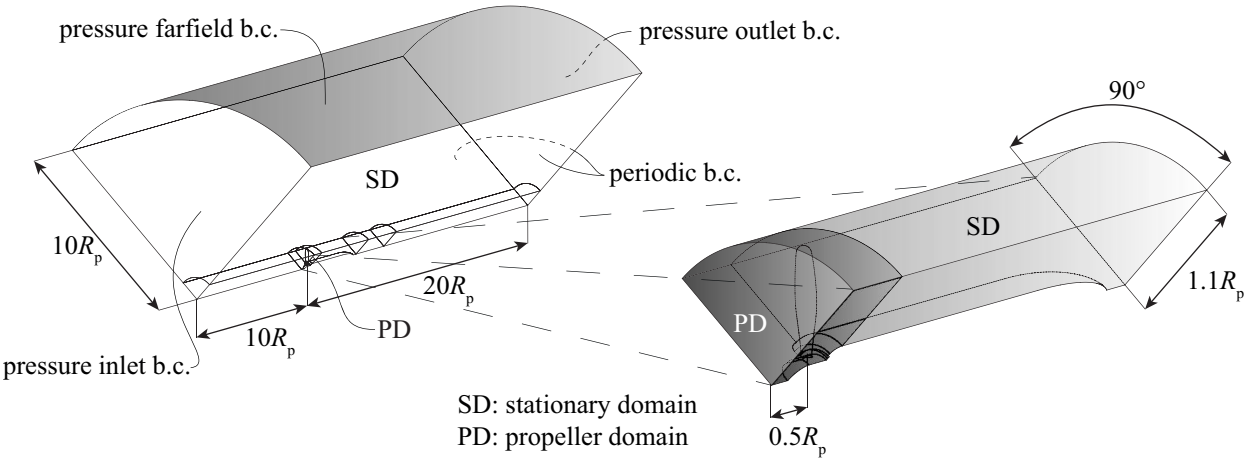

Fig. 5 Computational domain and boundary conditions for the isolated propeller configuration.

by a moving wall, being stationary in the absolute frame. On the sides of the domain, a conformal periodic boundary condition was specified to avoid interpolation and introduction of associated errors.

2. Wing and Propeller–Wing Configuration

The wing and propeller–wing configuration were installed in a domain representing the wind-tunnel test section. The computational domain is shown in Fig. 6. The upstream and downstream extent of the domain were chosen to match the inlet and outlet location for the isolated propeller configuration. The inlet and outlet boundary conditions were the same as for the isolated propeller configuration. The propeller blades, spinner, nacelle, wing and flap were defined as no-slip walls and the front part of the nacelle was again modeled by a moving wall. Part of the top wall of the wind-tunnel domain was also modeled as a no-slip wall to account for the interaction of the boundary layer of the wind-tunnel test section with the wing. All other wind-tunnel domain walls were set as slip walls. The entire inner domain could be rotated to model an angle of attack, after which remeshing of the wind-tunnel domain was needed. The flap could also be rotated to model a flap deflection, after which remeshing of the inner domain was required. Interfaces were present between the wind-tunnel domain, the inner domain and the propeller domain. To simulate the wing only or apply the actuator models, the propeller domain was replaced by a domain with only a spinner.

E. Grid and Grid Dependency Study

Grids were constructed by means of ANSYS® Meshing. For regions adjacent to no-slip walls, the unstructured grid was made up of a triangular wall mesh, followed by layers of semi-structured prismatic elements and tetrahedral elements. In the slipstream of both the isolated propeller and propeller–wing configuration an unstructured hexagonal mesh was used to reduce the grid size. Grid density in the whole domain was controlled by wall refinement of all no-slip walls, volume refinement of the domains, a 1st layer thickness of the inflation layers, and growth rates of the inflation layers and the remainder of the grid. The 1st layer thickness was tuned to comply with the y^+ requirement of the turbulence models of $y^+ < 1$. The only exception to this was the part of the no-slip wind-tunnel wall outside of the inner domain, for which wall functions were used. The number of inflation layers was tuned to encapsulate the boundary layer. The grids on periodic boundaries were conformal to avoid interpolation. For the propeller–wing configuration domain, the grid of the rotating domain was copied from the isolated propeller configuration and rotated to achieve periodicity in the grid.

A grid dependency study was performed for the isolated propeller and wing configurations. All refinements were varied systematically in the grid dependency study, except for the inflation layer which was kept constant in line with Roache [28]. To estimate discretization uncertainty, a least-squares version of the grid convergence index (GCI) as proposed by Eça and Hoekstra [29] was applied. Table 1 provides the grid size and refinement ratio h_i/h_1 for the five considered grids of the isolated propeller and wing configurations, where h_i is the average cell size of grid i and h_1 that of the finest grid. Grid 3 was the grid to be evaluated in this grid study. Richardson extrapolation of solutions ϕ_i on the five grids was performed by means of a least-squares approach. In case of oscillatory convergence or divergence, the

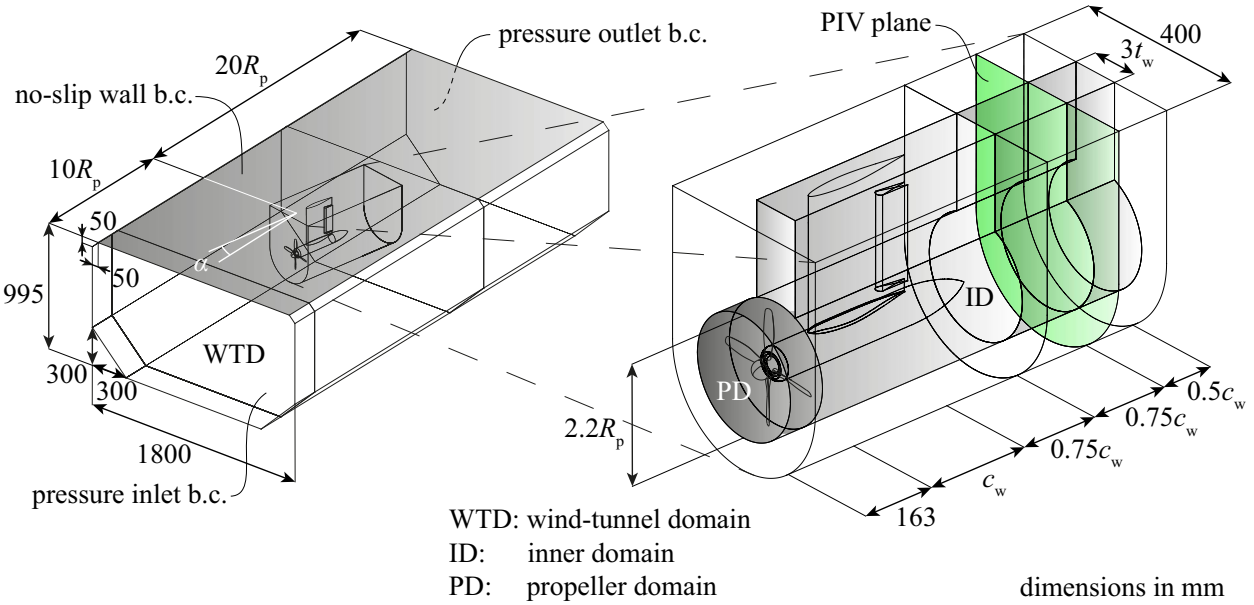

Fig. 6 Computational domain and boundary conditions for the wing and propeller–wing configuration.

least-squares approach cannot be followed and an error estimate based on the maximum difference of the solutions Δ_M was used. A small deviation from the method of Eça and Hoekstra [29] was introduced that only solutions on the chosen and more refined grids were evaluated to avoid penalizing evaluation of coarser grids:

$$\Delta_M = \max\left(\left|\phi_i - \phi_j\right|\right) \text{ with } 1 \le i \le n_{\text{chosen}} \wedge 1 \le j \le n_{\text{chosen}} \tag{4}$$

The resulting estimated error U_ϕ depends on the observed order of accuracy p and is:

$$U_\phi = \begin{cases} 1.25\delta_{\text{RE}} + U_{\text{s}} & \text{for } 0.95 < p < 2.05 \\ \min\left(1.25\delta_{\text{RE}} + U_{\text{s}}, 1.25\Delta_M\right) & \text{for } 0 < p < 0.95 \\ \max\left(1.25\delta^*_{\text{RE}} + U^*_{\text{s}}, 1.25\Delta_M\right) & \text{for } p \ge 2.05 \\ 3\Delta_M & \text{for } p < 0 \text{ or oscillatory} \end{cases} \tag{5}$$

where δ_{RE} is the difference between the estimated exact solution and the solution on the chosen grid, U_{s} is the standard deviation of the fit and δ^*_{RE} and U^*_{s} are based on a least-squares fit with the theoretical order of convergence ($p = 2$). This error analysis was performed for a number of quantities for the isolated propeller and wing configurations. Figure 7 displays convergence plots, showing the relative difference of the solutions with respect to the solution on grid 3 and fits based on the observed order and the theoretical order. Table 2 presents the corresponding observed order, standard deviation of the fits and estimated discretization error for grid 3. These results are discussed in the next two paragraphs.

Table 1 Grid sizes of the isolated propeller and wing configuration domain.

	isolated propeller configuration		wing configuration	
grid	# of cells	h_i/h_1	# of cells	h_i/h_1
grid 5	3,547,253	1.82	21,186,092	1.71
grid 4	4,529,662	1.68	27,771,270	1.57
grid 3	7,373,636	1.43	40,951,865	1.38
grid 2	12,451,486	1.20	63,484,270	1.19
grid 1	21,447,859	1.00	106,614,585	1.00

Table 2 Grid dependency study for the isolated propeller and wing configurations.

	isolated propeller configuration				wing configuration			
	$T'_{\max}$	$Q'_{\max}$	$u_{\max}$	$u_{0.7R_p}$	C_L	C_D	$(C_{p_t})_{\min}$ flap	$(C_{p_t})_{\min}$ wingtip
p	4.80	-	1.51	-	−5.05	5.42	-	3.10
U_s (%)	0.12	-	0.09	-	-	0.08	-	1.03
U_s^* (%)	0.15	-	0.17	-	-	0.13	-	1.16
$\lvert U_\phi \rvert$ (%)	1.14	0.16	9.75	0.82	1.09	1.02	0.20	16.02

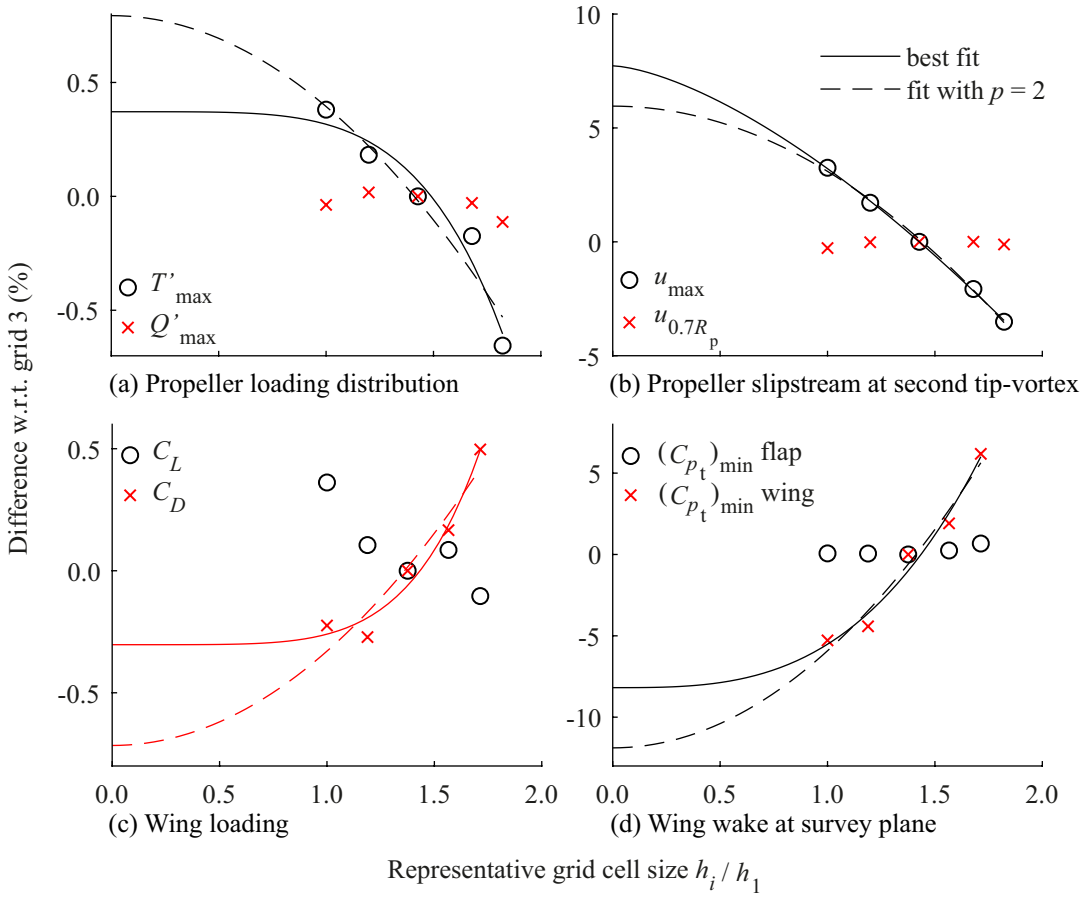

Fig. 7 Grid convergence plots for the isolated propeller and wing configurations.

1. Isolated Propeller Configuration

Grid convergence for the isolated propeller configuration was verified by analyzing the radial distributions of blade thrust and torque, and the axial velocity distribution in the slipstream. Figure 8 presents the radial thrust and torque distributions for the five considered grids. For all grids, the average loading distribution is plotted over the last 2 propeller rotations of a total of 4.5 rotations and for grid 3 also the spread over time is shown. The root section of the propeller blade is circular and transforms to an airfoil over the root part of the blade. This shape results in flow separation with time-varying loading. The maxima of the thrust and torque distribution, $T'_{\max}$ and $Q'_{\max}$, were chosen instead of the integrated loads to quantify the discretization uncertainty in order to avoid the noise due to the blade-root flow separation. For $T'_{\max}$, converging behaviour is found with an observed order of 4.80, resulting in the use of the theoretical order to estimate the discretization error. Note that the standard deviation of the fit with the theoretical

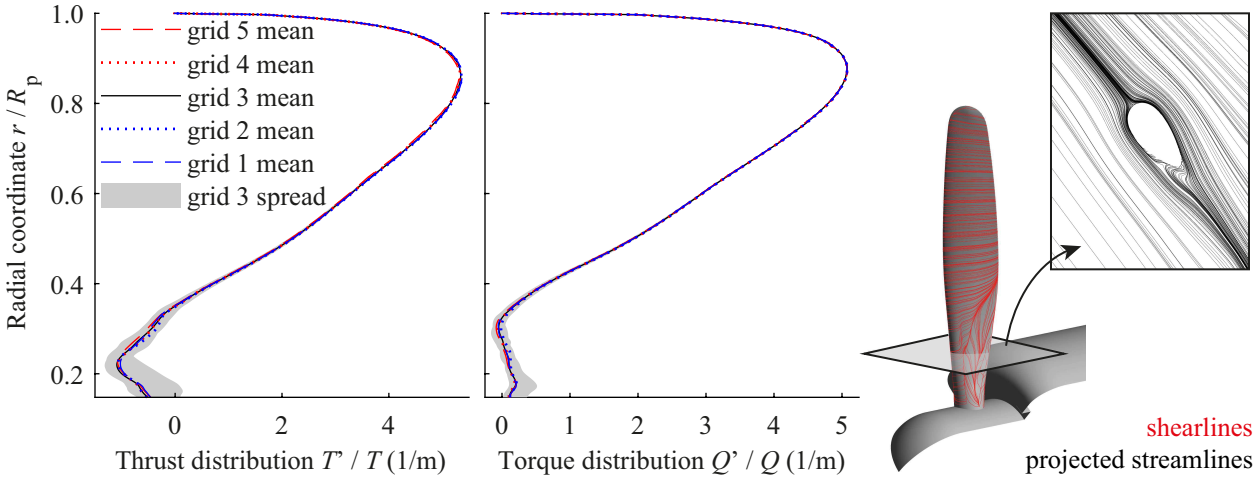

Fig. 8 Propeller blade radial thrust and torque distribution for the five considered grids. Shearlines on the blade and projected streamlines in the propeller reference frame on a plane at $r/R_p = 0.3$ show flow separation at the blade root.

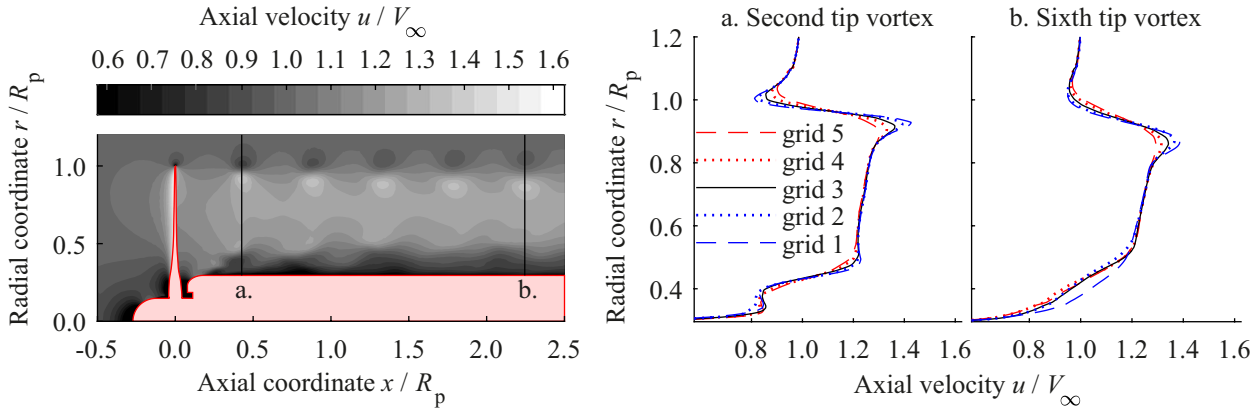

Fig. 9 Axial-radial contour plot through the blade pitch axis showing phase-locked axial velocity for grid 3. Radial profiles provide comparison with the other grids.

order is only marginally larger than that of the observed order and is relatively small, so a good fit was achieved. It is concluded that the propeller blade loading is converged well for grid 3, with a 1.1% estimated discretization error for T'_{max} and 0.2% for Q'_{max}, for which oscillatory convergence is observed.

To observe grid convergence for the axial velocity in the slipstream, a phase-locked contour plot of the axial velocity was constructed for each grid on an axial-radial plane through the blade pitch axis. In Fig. 9 this contour plot is presented for grid 3 and radial profiles through the second and sixth tip-vortex core are shown for all grids. In order to remove some of the unsteadiness stemming from the flow separation over the propeller blade root and from the front of the nacelle, again an average was taken over the last 2 propeller rotations of a total of 4.5 rotations. However, still some variation is present between the different grids in the region up to $r/R_p = 0.5$ as the result of this unsteadiness. Overall, the flowfield for grid 3 is converged well except in the tip-vortex region around $r/R_p = 1$, where the steep velocity gradients due to large local values of vorticity were not entirely captured as a result of numerical diffusion. The discretization error was estimated for the maximum axial velocity u_{max} and the axial velocity at $r/R_p = 0.7$ for the radial profile through the second tip-vortex. For u_{max}, an observed order of $p = 1.51$ was found, resulting in a relatively large discretization error of 9.8% for grid 3, while for $u_{0.7R_p}$ oscillatory convergence was observed with a much smaller discretization error of 0.8%. Unfortunately, the numerical methods found in typical low-order CFD solvers require extremely dense grids to avoid numerical diffusion and preserve the tip-vortex strength, resulting in excessively high computational cost [30]. Exploration of higher-order schemes for this type of flow and means of local grid refinement

were out of the scope of this paper, but will be addressed in future work. The qualitatively good agreement of the flowfield in the tip-vortex region and the quantitatively good agreement in the remainder of the slipstream of grid 3 compared to the denser grids were considered sufficient for the analysis discussed in this paper.

2. Wing Configuration

Grid convergence for the wing configuration was tested for the $\delta_f = +10°$ condition by evaluating the overall lift and drag coefficients, C_L and C_D. While the best fit for C_L was found to be divergent, the solutions for the large range of grid sizes are very close to each other and noticeable scatter is present, making this a poor fit. A discretization error of 1.1% was estimated for grid 3. For the drag coefficient, convergence was found resulting in a comparable discretization error of 1.0%.

A comparison of the total-pressure coefficient C_{p_t} in the wake of the wing at the location of the survey plane is presented in Fig. 10 for the different grids. A contour plot for grid 3 is given together with lateral total-pressure profiles, cutting the inboard and outboard flap-edge vortex, the flap wake at midspan and the wingtip vortex. Good agreement is found between the profiles of different grids outside the vortex cores. The minima in total pressure in the flap wake at midspan and in the wingtip vortex were analyzed quantitatively. Oscillatory convergence was observed for the flap wake with a marginal error of 0.2% for grid 3, while convergence was found for the total pressure in the core of the wingtip vortex with a large error of 16.0%. This latter error is again a result of numerical diffusion, although one should take into account that this error is presented with respect to the relatively low total-pressure coefficient in the vortex core; relative to the freestream total-pressure coefficient this error reduces to 5.8%.

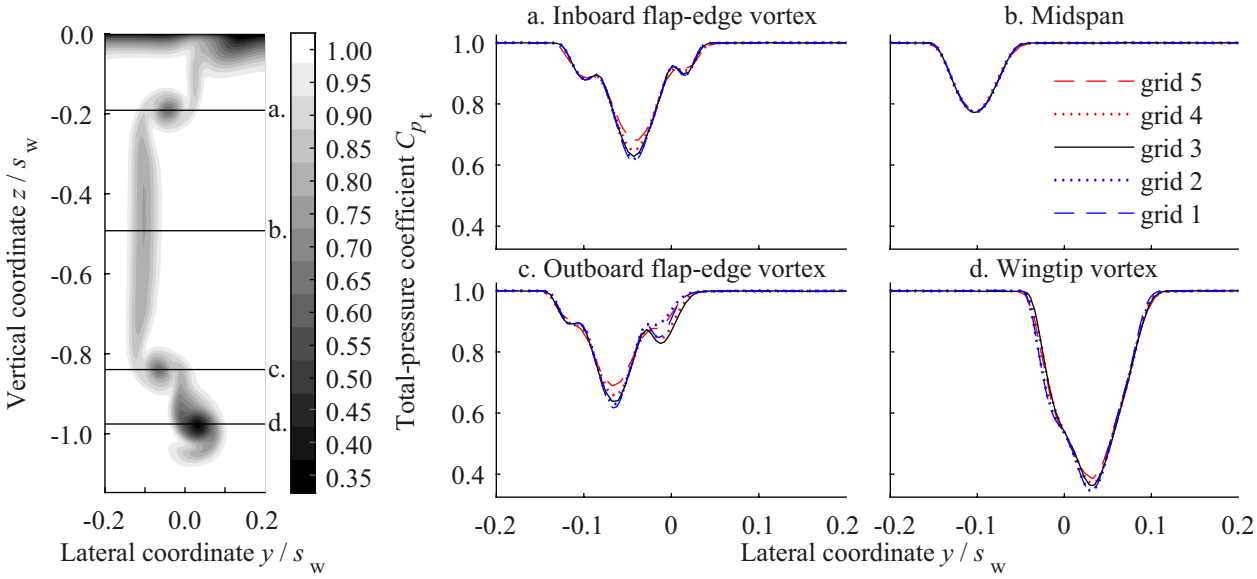

Fig. 10 Contour plot of the total-pressure coefficient in the survey plane for grid 3. Lateral profiles provide comparison with the other grids.

Based on the above grid dependency studies, it was concluded that grid 3 is well converged in terms of propeller and wing loading, slipstream flowfield, and wing wake, except for the vortex cores where a considerable discretization error needs to be taken into account. Therefore, grid 3 was used for the results presented in the remainder of the paper.

IV. Comparison of Computational and Experimental Results

The results obtained using the full-blade model and actuator models were compared to the experimental data to validate the full-blade model and quantify the error introduced by the actuator models. For all configurations the blade loading distributions were extracted from the full-blade model results and supplied to the actuator models.

A. Isolated Propeller Configuration

The purpose of the analysis of the isolated propeller configuration is to compare and validate propeller modeling without the interaction with the wing. Differences in modeling without interaction should become clear to later differentiate from differences due to interaction with the wing. To this end, a comparison was made of the time-averaged total pressure and phase-locked axial velocity in the slipstream. Figure 11 presents the radial variation of total-pressure coefficient, averaged over the circumference just downstream of the propeller disk at $x/R_\mathrm{p} = 0.19$. In the experiment a total-pressure measurement was performed by traversing a total-pressure probe in the radial direction at the vertical position of the propeller axis. Comparing the results of the full-blade simulation and the experiment, good qualitative agreement is found in the total-pressure profile. The main differences visible are a higher maximum in total pressure in the experiment in the region $0.5 < r/R_\mathrm{p} < 0.9$ and a steeper total-pressure gradient near the nacelle and at the slipstream edge. The quantitative difference in the maximum with respect to the experiment is given in Table 3 and is found to be -3.1% for the full-blade model. These differences are likely not a result of a model error in the propeller blade loading, but are thought to be due to the numerical diffusion of the blade tip and root vortices in the CFD simulations, as discussed in Section III.E.1. This results in a slight reduction in contraction of the slipstream compared to the experiment as is visible in Fig. 11, but not in a reduction of momentum in the slipstream. The lack of change in momentum in the slipstream was confirmed by analysis of the integral of total pressure over the evaluation disk, which was found to be approximately 1% from the experiment for all models as reported in Table 3. Comparing the actuator-model results with the full-blade result, minor deviations are observed, especially near the nacelle in the region $0.3 < r/R_\mathrm{p} < 0.45$. These deviations are the result of two differences between the full-blade and actuator models. First, only the time-average blade loading is prescribed in the actuator models, while flow separation on the root part of the blade results in time-varying loading as was shown in Fig. 8. Second, neglecting the finite thickness of the blade in the introduction of momentum and energy sources for the actuator models may have resulted in a different interaction with the front of the nacelle because of its close proximity.

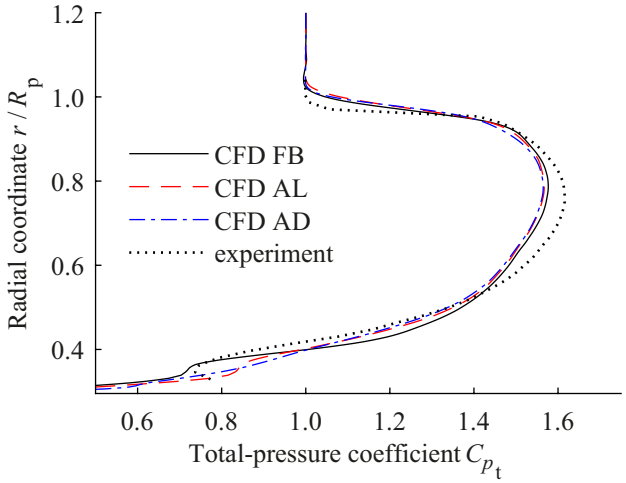

Fig. 11 Radial variation of total-pressure coefficient averaged over the circumference at $x/R_\mathrm{p} = 0.19$.

Table 3 Difference in C_{p_t} quantities from Fig. 11 with respect to the experimental data.

difference of	CFD FB	CFD AL	CFD AD
C_{p_t} integral (%)	−0.81	−0.85	−1.22
C_{p_t} maximum (%)	−3.08	−3.68	−3.82

The time-dependent agreement of the full-blade and actuator-line model slipstream with that of the experiment can be observed in Fig. 12. Contour plots of the phase-locked axial velocity in the slipstream are shown for the actuator-line

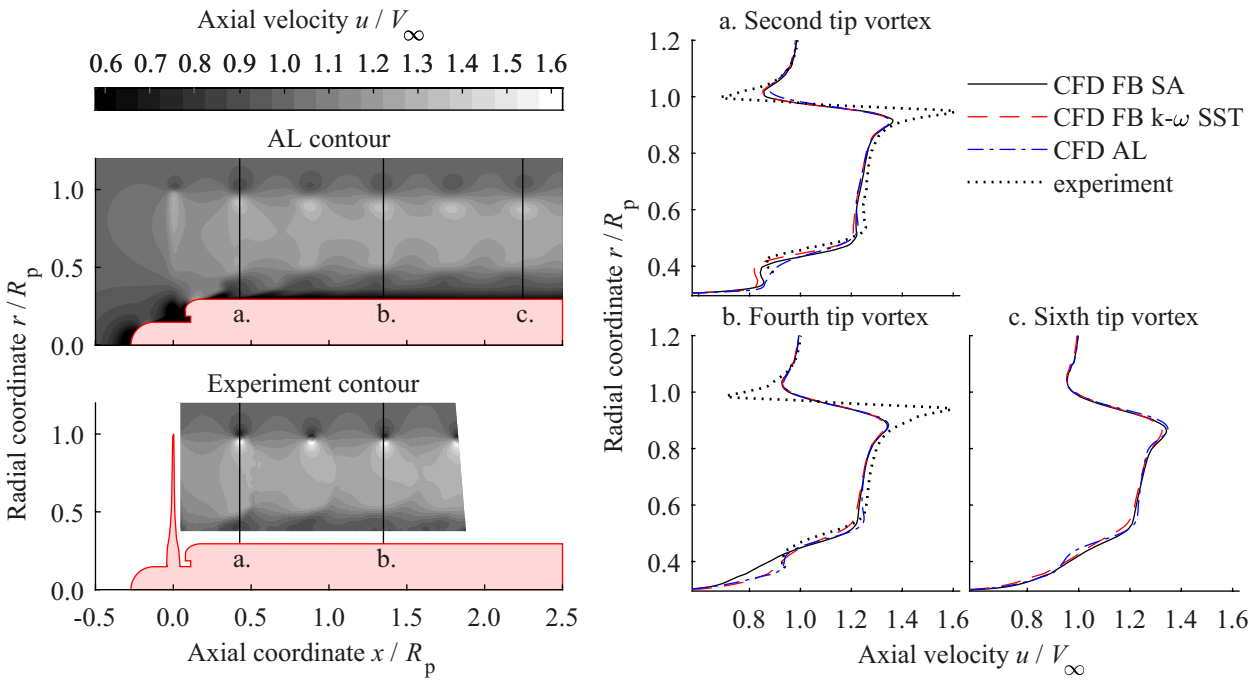

Fig. 12 Axial-radial contour plots through the blade pitch axis showing the phase-locked axial velocity for the actuator-line model and experiment. Radial profiles provide comparison with the full-blade model.

model and for the experiment obtained by PIV. The contour plot obtained for the full-blade model was shown before in Fig. 9. Furthermore, radial profiles through three tip vortices provide a quantitative comparison of the results. For the full-blade model not only results obtained with the Spalart–Allmaras (SA) turbulence model are shown, but also with the $k-\omega$ SST turbulence model. The main difference between the CFD results and the experiment is the reduced axial velocity maximum and minimum in the tip vortices in the CFD results. In the grid dependency study a discretization error of 9.8% was found for the maximum of the axial velocity for the profile through second tip vortex, as a result of numerical diffusion (Section III.E.1). Based on the extrapolated grid value, a model error for the full-blade model with respect to the experiment remains of 7.0% in the second tip vortex core. Outside the tip vortices a good match is observed with the same differences visible as for the total-pressure coefficient in Fig. 11. No large effect of the turbulence model is found for the plotted range, although it was observed that further downstream in the same plane the velocity gradients in the tip vortices for the $k-\omega$ SST model kept decaying while they remained constant at the level of the sixth tip vortex for the SA model. Comparing the actuator-line model with the full-blade model, it is observed that a good match is obtained in terms of the time-dependent flowfield.

B. Wing Configuration

The wing loading and characteristics of the wing wake obtained for the wing configuration were assessed to validate wing modeling without propeller interaction. The overall loading on the wing and nacelle including turntable were obtained by balance measurements in the experiment. This allowed a comparison of the overall lift and drag coefficient with the CFD results. The C_L and C_D are given in Table 4 for the wing configuration with $\delta_f = \pm 10°$. For the CFD simulation the SA turbulence model was used. While the lift for the positive and negative flap deflection should be exactly the opposite, for the experiment this was not the case. The likely reason is a small misalignment of the wing and the nacelle in the angle of attack. The lift coefficient found from the CFD simulation is in between these values. The drag coefficient is slightly higher for the CFD result compared to the experiment, which is expected due to the fully turbulent modeling of the boundary layer, compared to the forced transition at $x'/c_w = 0.12$ in the experiment. The drag is relatively high for the given lift, because it includes the drag of the turntable of about 1/3 of the total. In the remainder of this section results are shown only for $\delta_f = +10°$.

To get more insight in the agreement of the CFD results and the experiment, Fig. 13 displays the chordwise pressure distributions at the flap midspan and near the outboard flap edge. Coordinate x' changes with flap deflection as depicted in Fig. 2. For the flap at the midspan location also streamlines are shown. Again, both the SA and $k-\omega$ SST turbulence models are considered in the comparison with the measured data from the experiment. Very good agreement is found

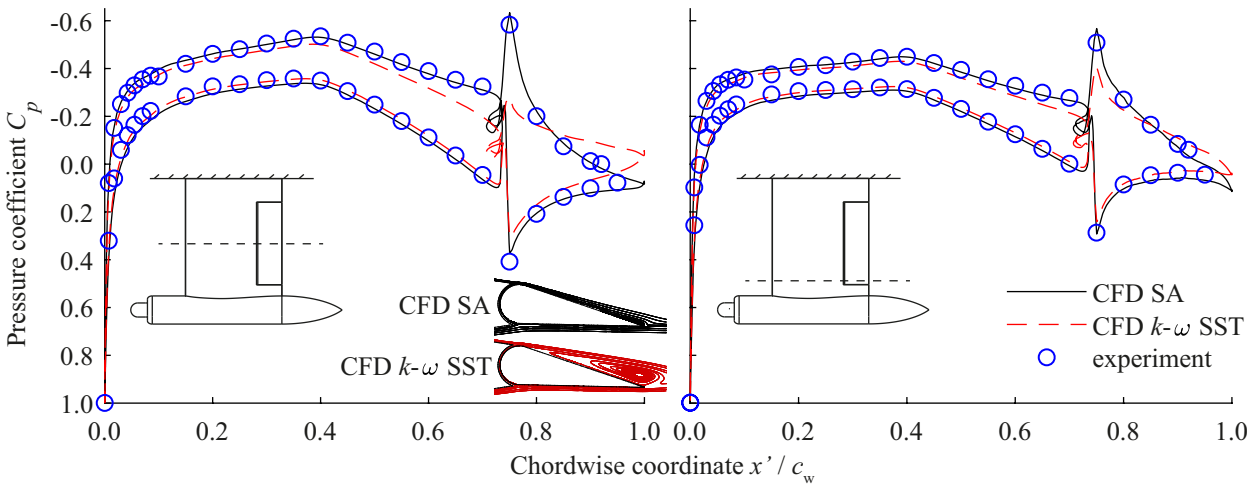

Fig. 13 Pressure distributions at the flap midspan and near the outboard flap edge, δ_f = +10°.

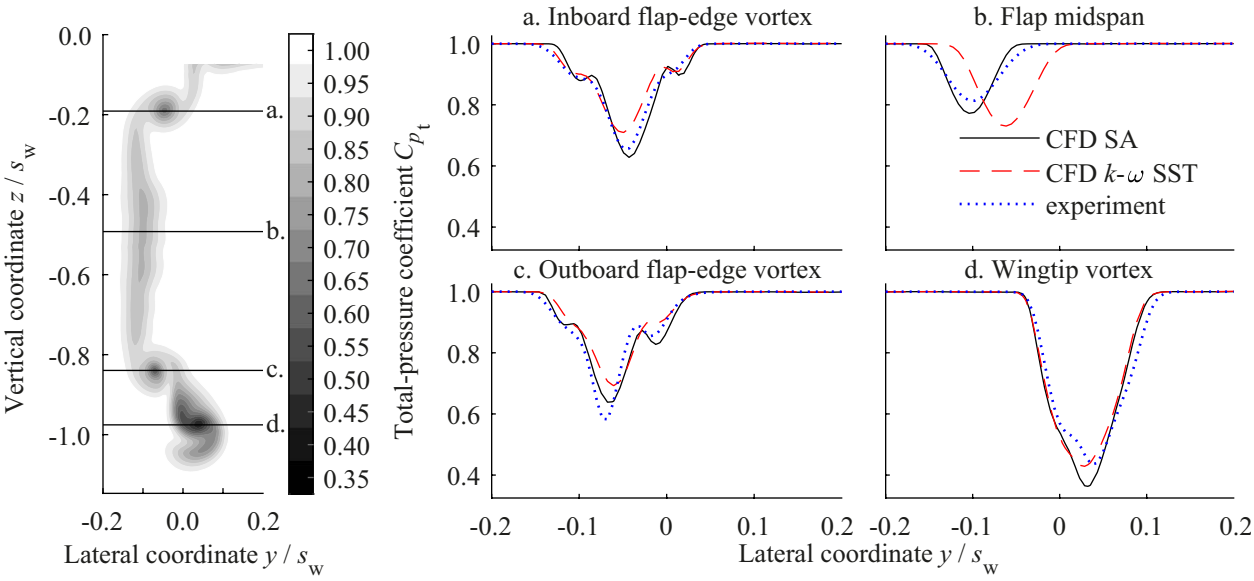

Fig. 14 Total-pressure coefficient contour plot obtained in the experiment at the survey plane, δ_f = +10°. Lateral profiles provide comparison with CFD results.

between the CFD results computed with the SA turbulence model and the experimental data. A small difference is present on the suction side around $x'/c_w = 0.12$ where the upstream effect of the transition strip results in a slight increase in pressure for the experiment. The pressure distributions for the $k-\omega$ SST turbulence model at the flap midspan section deviate over the entire suction side of the flap due to flow reversal, as shown by the streamlines. Flow reversal occurred to a lesser extent for the section near the flap edge.

To validate the characteristics of the wing wake, a comparison of the total-pressure coefficient C_{p_t} in the wake of the wing at the location of the survey plane is presented in Fig. 14. For the experimental data a contour plot is shown and lateral total-pressure profiles are plotted including CFD results for both turbulence models. These profiles run through the inboard and outboard flap-edge vortex, the flap wake at midspan and the wingtip vortex. The corresponding CFD contour plot obtained with the SA turbulence model was shown before in Fig. 10. Comparing the CFD SA and experimental results in the contour plots, very good agreement in the total-pressure deficit distribution is found, matching closely the location of the flap vortices, the wingtip vortex and the wing wake. Note that at $z/s_w = 0$ a boundary layer is formed on the reflection plane of the wind tunnel section, which is only visible in the CFD results since no total-pressure measurement could be performed in that region. The lateral total-pressure profile shows that the flap wake is slightly wider and the total-pressure deficit slightly larger in the CFD SA result compared to the experiment. Again, this is likely due to the fully turbulent modeling of the wing compared to the experiment. For the $k-\omega$ SST

Table 4 Overall lift and drag coefficients obtained with the SA turbulence model for the wing and the propeller–wing configuration. The full-blade propeller model is used.

		wing configuration		propeller–wing configuration	
		$\delta_f = +10°$	$\delta_f = -10°$	$\delta_f = +10°$	$\delta_f = -10°$
CFD	C_L	0.200	−0.200	0.259	−0.180
	C_D	0.041	0.041	−0.173	−0.167
experiment	C_L	0.189	−0.205	0.257	−0.180
	C_D	0.040	0.040	−0.180	−0.177

turbulence model, the lateral location of the flap wake is offset from the experiment and the difference in total-pressure deficit is even larger, both a direct result of the flow reversal on the suction side of the flap for this turbulence model. The reduced pressure difference between the suction and pressure side for the $k-\omega$ SST turbulence model (Fig. 13) is also visible in the lower total-pressure deficit of the flap vortices, while with the SA turbulence model closer agreement with the experiment is found. The wingtip vortex is slightly better modeled by the $k-\omega$ SST turbulence model, although both turbulence models show a similar reduced pressure deficit compared to the experiment. This is partially a discretization error due to numerical diffusion as was shown in the grid dependency study (Section III.E.2). Note that numerical diffusion also affected the strength of the flap-edge vortices.

C. Propeller–Wing Configuration

The propeller–wing configuration was assessed for two flap deflections of $\delta_f = +10°$ and $\delta_f = -10°$ in terms of wing loading and wake flowfield. All full-blade and actuator-line results were obtained by taking the average over the last rotation of a total of 6.25 rotations, while the actuator-disk results were converged to a steady state. The SA turbulence model was selected based on the comparison of turbulence models for the wing configuration and isolated propeller configuration. For the wing configuration it was concluded that the SA turbulence model predicted flow separation on the flap better than the $k-\omega$ SST turbulence model and therefore also predicted the wake better. For the isolated propeller model less decay was observed of the velocity gradients in the tip vortices with downstream direction.

The effect of the propeller on the overall lift and drag coefficient can be observed in Table 4 for the full-blade model and the experiment. Compared to the results for the wing configuration, the lift coefficient for the positive and negative flap deflection changes by a positive increment due to the combined effect of the swirl and dynamic pressure increase in the slipstream. The lift coefficient obtained for the CFD and experiment are very similar. The drag coefficient becomes negative, since the thrust of the propeller is included and is much larger than the wing and nacelle drag. For both flap deflections, the drag coefficient predicted by the CFD simulation is somewhat less negative than that from the experiment. This is for a large part explained by the choice of grid and the corresponding discretization error in the propeller thrust and wing drag as discussed in the grid dependency study. To get a better insight into the agreement and differences between the CFD models and the experiment, the pressure distributions on the wing and the flowfield behind the wing were investigated.

The time-averaged effect of the propeller slipstream on the wing loading and the effect of the direction of the flap deflection are both noticeable in the pressure distribution near the outboard flap edge presented in Fig. 15. Compared to the case of the isolated wing (Fig. 13), a suction peak is present near the leading edge as a combined result of the swirl and dynamic pressure increase in the slipstream. Note that the pressure coefficient in the stagnation point is larger than unity since the section is located in the slipstream, while the freestream dynamic pressure is used to define the pressure coefficient. For both flap deflections a good match is found between the measurements and the CFD results for all propeller modeling methods. However, over the majority of the suction side, a slightly lower pressure is noticeable for the actuator-disk model compared to the other two CFD results. This lower pressure is also reflected in the lift and drag distributions over the entire half span, shown in Fig. 16 for the positive flap deflection. While the actuator-line and full-blade model results are almost the same, a slightly increased lift coefficient is shown for the actuator-disk model at all spanwise sections except on the nacelle. The corresponding increase in integrated lift coefficient over the halfspan compared to the full-blade model is 3.9%. However, almost no change in drag coefficient is present, except a reduction at the nacelle. Apparently, the time-averaged effect of the swirl on the wing loading is slightly larger with the actuator-disk model than with the full-blade and actuator-line representations of the propeller. Since the actuator-disk and actuator-line models are based on the same propeller blade loading distributions, the time dependency of the slipstream is the expected origin of the difference in lift distribution. Apparently, the time-average of the unsteady response of the wing to the slipstream is not equal to the response of the wing to the time-averaged slipstream. A

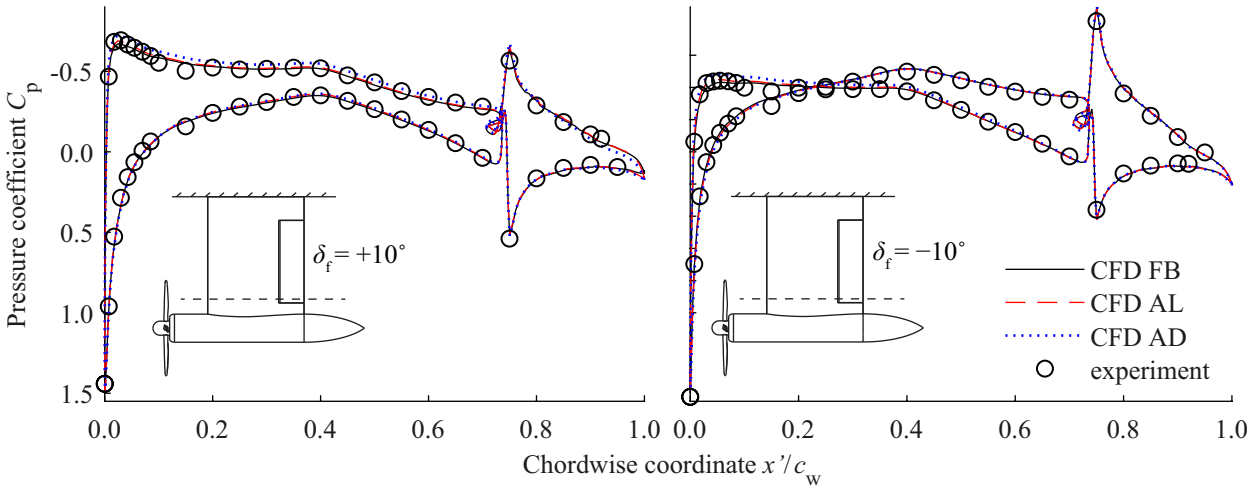

Fig. 15 Time-averaged pressure distributions at a section near the outboard flap edge, $\delta_f = \pm 10°$.

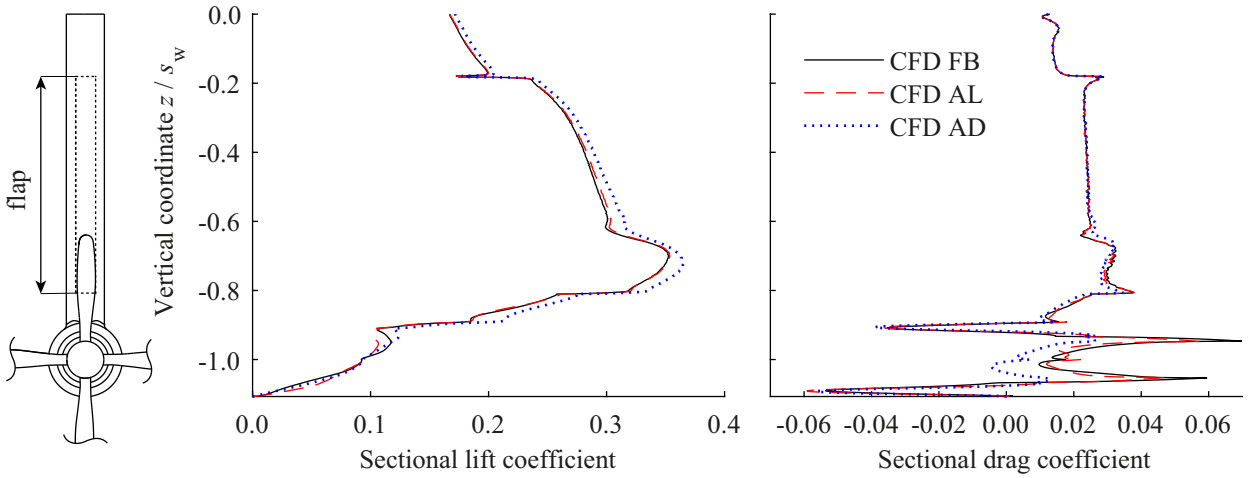

Fig. 16 Time-averaged spanwise lift and drag distribution, $\delta_f = +10°$.

similar observation was made by Thom and Duraisamy [31], where the inviscid response of a wing to an unsteady and time-averaged slipstream was compared for a midspan located tractor propeller. The only other reason for the difference in lift distribution of the actuator-disk model could have been transient wing loading effects caused by for instance flow separation, which were not correctly captured in the steady-state solution. This was checked with a transient simulation of the actuator-disk model, but no difference in wing loading was found compared to the steady-state solution.

The difference between the steady and time-accurate response of the wing can be observed in Fig. 17. The inherently steady pressure distribution of the actuator-disk model is compared to the time-accurate results for the other two models at the spanwise section where the propeller blade tip-vortices impinge on the wing. The location of the impinging helical vortex system is visualized by isosurfaces of positive and negative tangential vorticity component as computed with the actuator-line model. In the positive tangential vorticity isosurface a clear axial deformation is visible between the wing suction and pressure side. Moreover, a deformation in spanwise direction occurs, which was also observed by Sinnige et al. [16] At each tip-vortex core, a suction peak is noticeable in the pressure distribution on both sides of the airfoil. The locations as well as the magnitudes of these suction peaks agree well for the full-blade and actuator-line model and thus the helical tip-vortex system and its deformation match well.

The next step is the validation of the flowfield behind the wing. This is relevant because it is the result of the interaction of the slipstream with the wing and can give further insight in this interaction. A comparison of the total-pressure coefficient C_{p_t} in the wake and slipstream at the location of the survey plane is presented in Fig. 18 for $\delta_f = +10°$. Alongside, radial total-pressure profiles are plotted for two azimuthal locations. In all contour plots, the increased total pressure in the slipstream is visible, masking part of the flap wake. In general, the full-blade model result agrees well with the experiment. Differences are visible in the area of reduced total-pressure in the core of

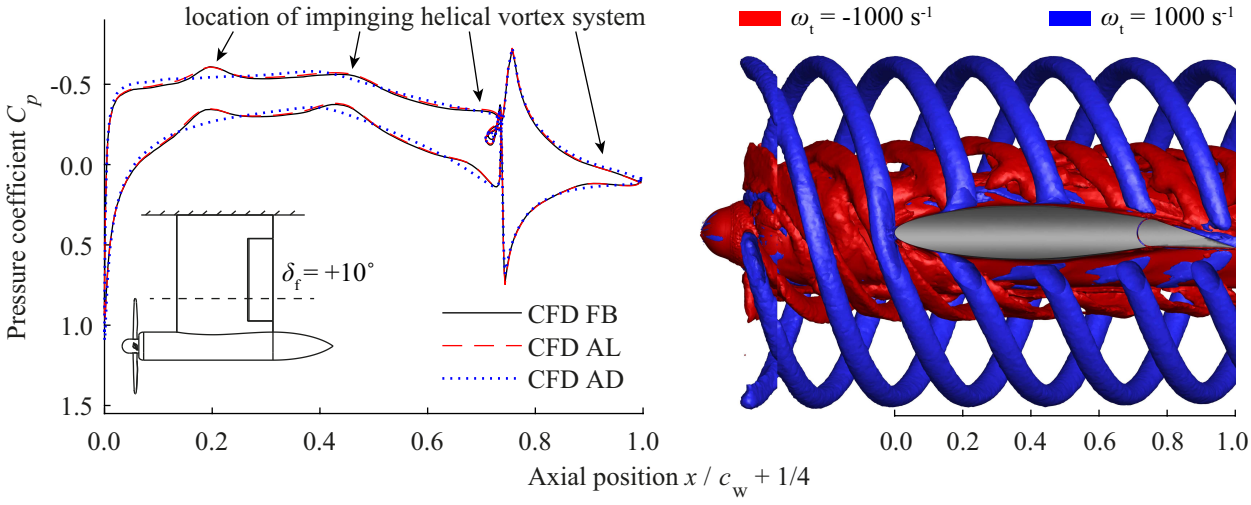

Fig. 17 Time-accurate (FB and AL) and steady (AD) pressure distribution at the slipstream edge at r/R_p = 0.99, δ_f = +10°. Tangential vorticity isosurfaces indicate location of impinging helical vortex system.

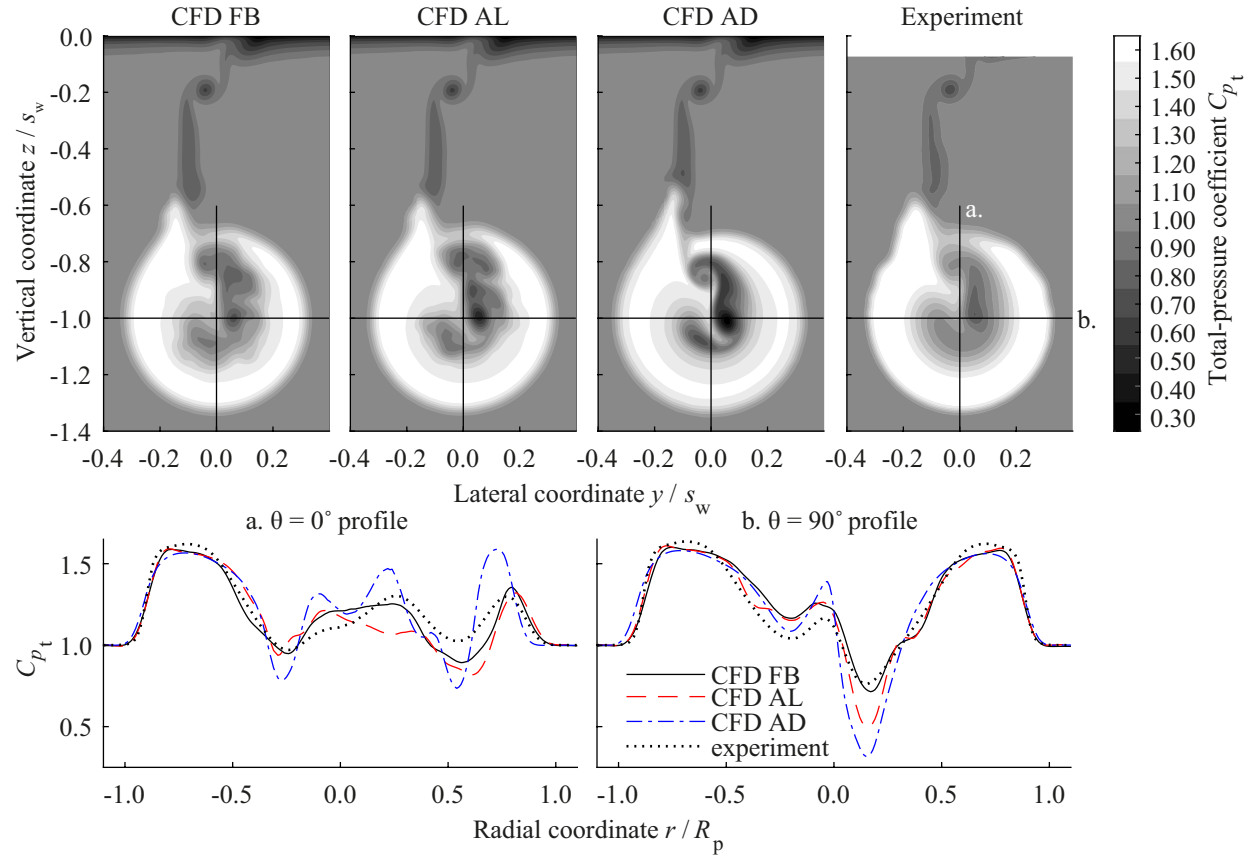

Fig. 18 Time-averaged total-pressure coefficient at the survey plane, δ_f = +10°.

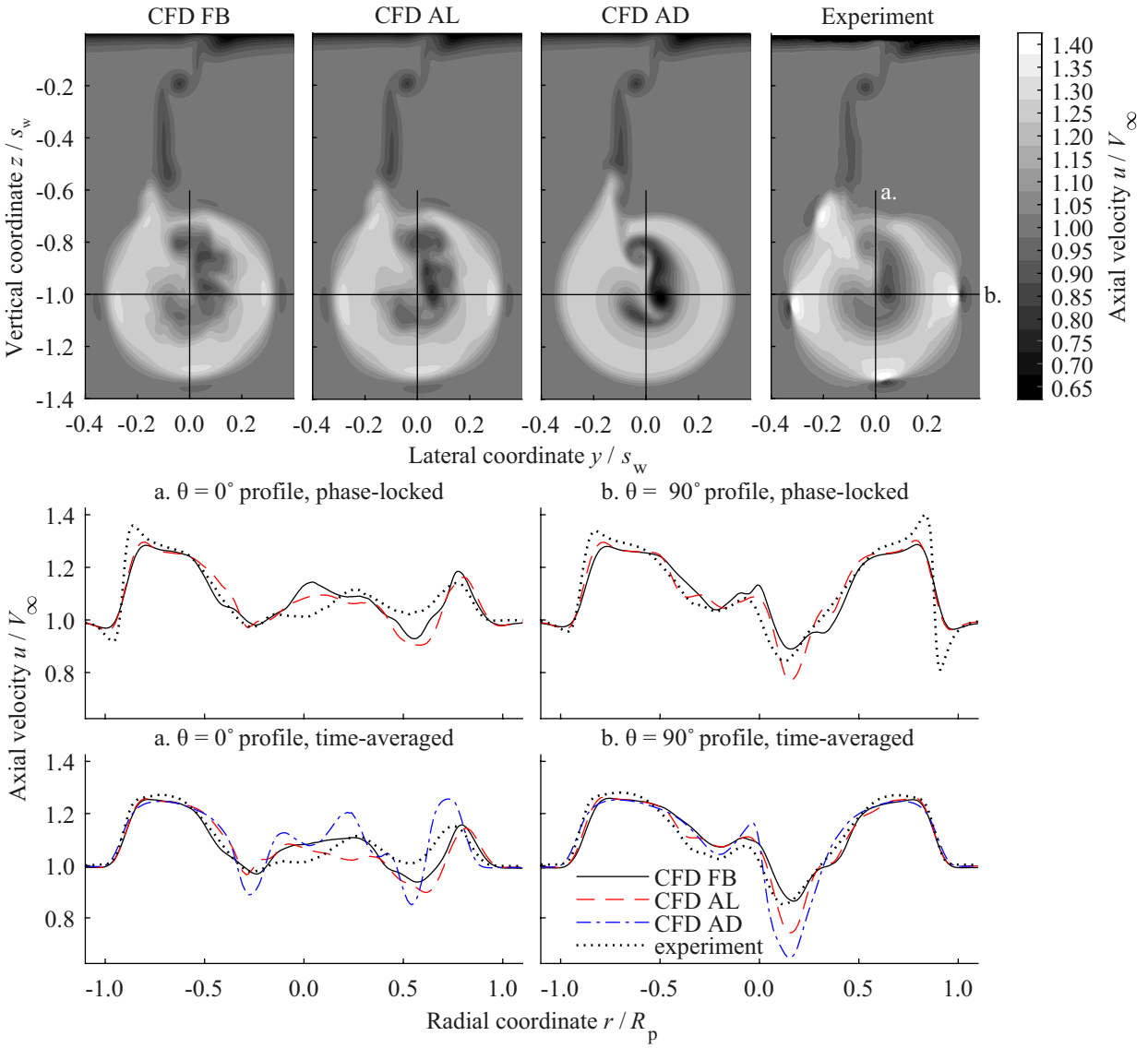

Fig. 19 Phase-locked and time-averaged axial velocity at the survey plane, δ_f = +10°.

the slipstream. This area is influenced by vortex shedding from the root of the propeller blades and the front of the nacelle due to flow separation. The averaging time was slightly too short to properly capture the time-average of these phenomena in the simulations. Furthermore, a slightly lower total pressure can be observed in the outer part of the slipstream for the full-blade model compared to the experiment. This difference was already present for the isolated propeller and was thought to be a result of decreased contraction due to the decay of the tip vortices in the simulations as explained in Section IV.A. The wingtip vortex is identified by the largest pressure deficit in all contours and the outboard flap-edge vortex is also still visible. For the actuator-disk model, these vortices are more clearly recognizable than for the other methods and the experiment. The pressure deficit in the wingtip vortex is also larger, especially compared to the full-blade model and experiment. Two effects play a role. First, the higher wing loading for this model (Fig. 16) results in a stronger tip vortex with larger pressure deficit. Second, the time-dependent vortex field shed from the propeller for the other methods and the experiment may result in a time-dependent interaction with the wingtip vortex, moving the vortex location over time, and thus showing up as a reduced pressure deficit over a wider area in these time-averaged contours. Since time-averaged blade loading is used for the actuator-line model, less variation in the vortex shedding is present for this model, and this may be the reason for its larger total-pressure deficit.

The phase-locked PIV data provide the opportunity to also compare the time-dependent flowfields in the wake and slipstream. Phase-locked contour plots for all propeller modeling methods and the experiment are shown in Fig. 19 for the axial velocity, except for the actuator-disk model for which a time-averaged contour is plotted, since no time-accurate data can be obtained with this model. Radial profiles for both the phase-locked and the time-averaged axial velocity

Table 5 Ratio of rotational to total kinetic energy flow through the survey plane in the propeller reference frame, integrated up to $r/R_p = 1.1$.

	$\Delta E_{k_{rot}}/\Delta E_{k_{tot}}$ (%)	
	$\delta_f = +10°$	$\delta_f = -10°$
full-blade model	1.04	4.92
actuator-line model	1.15	4.80
actuator-disk model	1.15	4.59
experiment	0.88	5.37

are provided as well. The phase is chosen such that a tip vortex aligns with the 90° radial profile. Observing the time-averaged profiles first, exactly the same deviations are found as compared to those for the total-pressure coefficient presented in Fig. 18, both in terms of the comparison of the experiment with the numerical results and the comparison between the full-blade and actuator-line simulations. In the phase-locked contours, a good qualitative agreement is observed, with the locations of the blade-tip vortices for the full-blade and actuator-line model simulations matching well with the experiment. However, the phase-locked profiles and contour plots reveal again the large difference in the velocity gradients in the blade-tip vortex cores between the CFD and experimental results.

So far, results of the flowfield in the wake and slipstream have been shown for a positive flap deflection of $\delta_f = +10°$, where the slipstream swirl goes against the direction of rotation of the wingtip vortex. This is the most relevant case for wingtip mounted propellers, since it is beneficial in terms of wing induced drag. The other case where the swirl turns in the same direction as the wingtip vortex is simulated by means of a negative flap deflection of $\delta_f = -10°$ and provides the opposite interaction. This becomes clear in the time-averaged tangential velocity component in the slipstream as provided in Figs. 20 and 21 respectively. For all propeller modeling approaches and the experiment, the tangential velocity in the slipstream is lower for the positive flap deflection than for the negative flap deflection. The rotation of the flow around the wingtip as a result of the pressure difference between the suction and pressure side opposes the propeller swirl for the positive flap deflection, while the opposite occurs for the negative flap deflection. As a combined result of the gradients in the spanwise wing-loading distribution and the rotation of the flow around the wingtip, a spanwise shearing of the slipstream occurs. This shearing is also visible in the contours of tangential velocity and is found to be stronger for the negative flap deflection, since the two effects amplify each other, while they oppose each other for the positive flap deflection [16]. Very similar flowfields are obtained with the propeller models compared to the experiment. The main difference for the positive flap deflection (Fig. 20) is found in the tangential velocity in the wingtip vortex, which shows a more negative tangential velocity for the actuator-line and especially actuator-disk models. This is again thought to be a difference due to reduced movement of the wingtip vortex due to reduced time dependence of propeller blade vortex shedding as explained for the total-pressure coefficient in Fig. 18.

For the negative flap deflection (Fig. 21), an additional difference of the experiment compared to all propeller models is found in the inboard part of the slipstream, where an area with considerably higher tangential velocity is located. This is discussed in more detail by van Arnhem et al. [15] In order to explain it, the interaction of the tip vortices with the wing should be considered first. As shown in Fig. 17 and also explained Refs. [16] and [31], the propeller tip vortices deform upon impact with the leading edge of the wing. For the advancing blade side of the wing, this results in an increase in the axial vorticity component of the tip vortices, while on the retreating blade side the axial vorticity is decreased to the extent that it changes sign. While in the survey plane the tip vortices change location over time and therefore do not show up clearly in the time-averaged tangential velocity contour plots, these deformed vortices trail downstream of the flap in mostly the axial direction. Therefore, they have a fixed location in the survey plane, resulting in a concentrated effect in the contour plots. Together with the outboard flap-edge vortex, which consists of mainly an axial vorticity component of negative sign, a strong positive tangential velocity is induced. The effect of these vortices is much less visible for the CFD results, likely due to numerical diffusion.

The significance of the deviations in the flowfield between the CFD results and the experiment is best observed in the integral of the kinetic energy flow through the survey plane. In Table 5 the ratio of rotational and total kinetic energy flow is given for $\delta_f = \pm 10°$. Note that the kinetic energy is only the addition of kinetic energy to the flow. The kinetic energy flow is calculated in the propeller reference frame and integrated up to $r/R_p = 1.1$. Although the ratio of rotational to total kinetic energy is not exactly the same for all propeller modeling methods on the one hand and the experiment on the other hand, the change of this ratio from about 5% to about 1% by the change in the flap deflection is observed for all modeling methods and the experiment. The clearly reduced swirl loss for propeller rotation against the direction of the wingtip vortex, shows the importance of rotation direction for tip-mounted propellers.

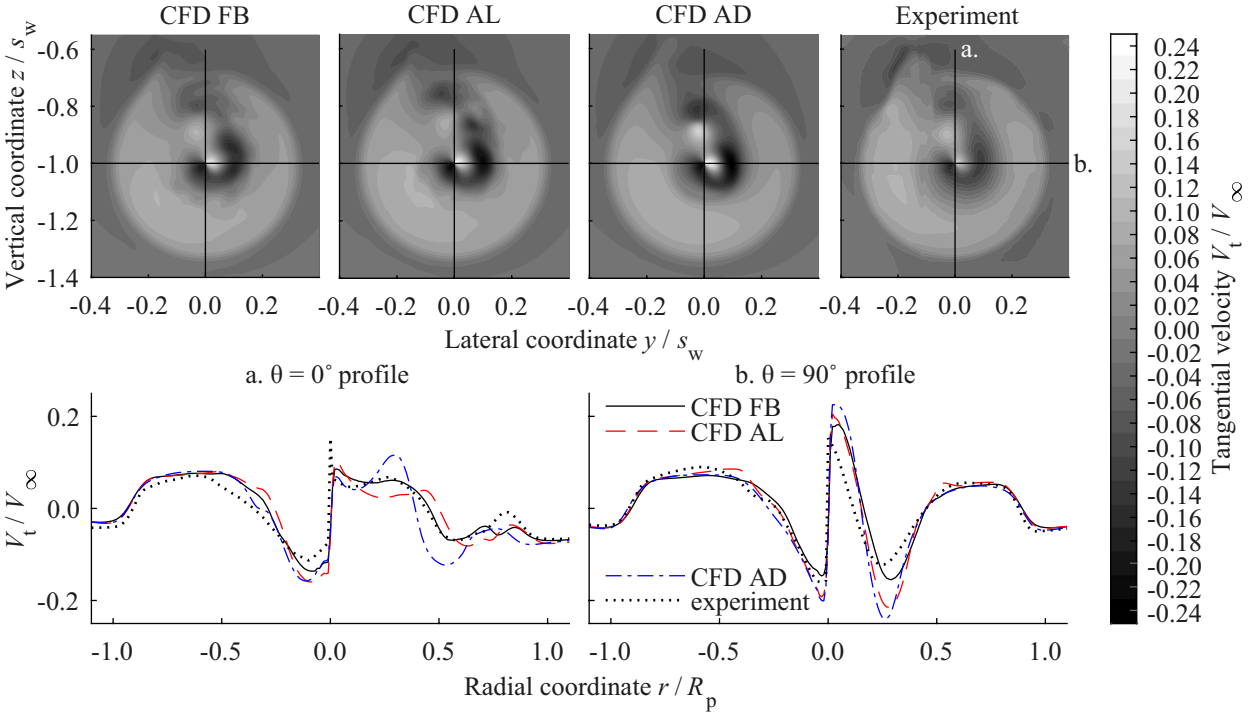

Fig. 20 Time-averaged tangential velocity in the propeller reference frame at the survey plane, $\delta_f = +10°$.

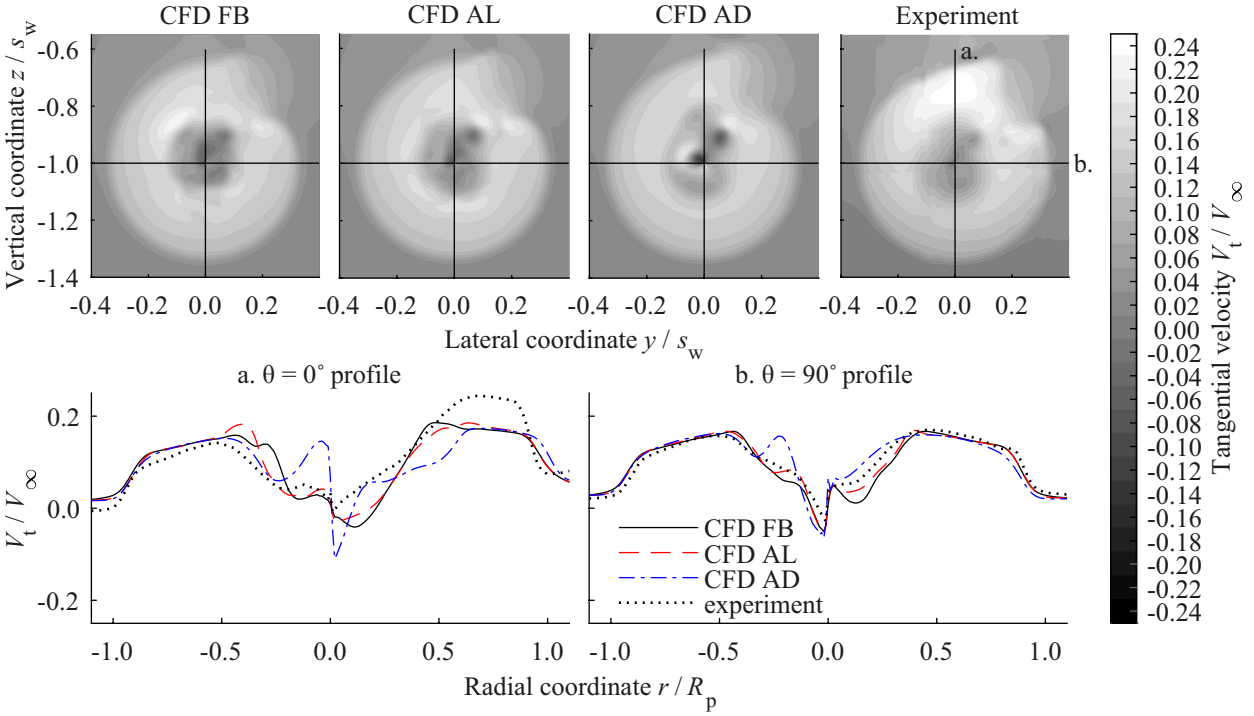

Fig. 21 Time-averaged tangential velocity in the propeller reference frame at the survey plane, $\delta_f = -10°$.

V. Conclusion

This paper has provided a comparison of full-blade propeller simulations with a wind-tunnel experiment of a wingtip-mounted propeller in tractor configuration. Furthermore, two reduced order models for the propeller have been tested: the actuator-line and actuator-disk models. In order to distinguish modeling errors of the propeller and wing simulations from modeling errors of their interaction, also the isolated propeller and wing have been investigated. The following conclusions were drawn for the propeller model:

- Numerical diffusion of the flow quantities in the propeller tip vortices was the only significant source of difference between the full-blade model and experiment, also resulting in a reduction in contraction for the full-blade model.
- The Spalart–Allmaras turbulence model only showed differences from the $k-\omega$ SST turbulence model for the downstream extent of the slipstream from $x/R_\mathrm{p} = 2.25$, where numerical diffusion in the vortex cores for the SA model was less.
- The actuator-disk and actuator-line models provided an accurate time-averaged slipstream, only deviating from the full-blade model close to the nacelle. This is thought to be due to the difference in modeling the close interaction of the blade root and nacelle by neglecting the blade thickness and due to the lack of the time dependence of the flow separation from the blade root in both models.
- The actuator-line model agreed almost one-to-one with the full-blade model in a time-accurate sense.

For the wing model the following conclusions were drawn:

- Accurate agreement in integrated lift and drag was found for the CFD model with Spalart–Allmaras turbulence model and the experiment. The main difference was a result of a small misalignment of the wing and nacelle in the experiment.
- The Spalart–Allmaras turbulence model predicted flow separation on the flap far better than the $k-\omega$ SST turbulence model, also resulting in a better match of the wake in terms of total-pressure coefficient. Both turbulence models suffered from reduced total-pressure gradients in the vortex cores due to numerical diffusion.

At last, the following conclusions were drawn for the propeller–wing model:

- Accurate agreement of the time-averaged pressure distributions on the wing in the slipstream were obtained by the full-blade and actuator-line model compared to the experiment, in line with the good agreement obtained for the integrated lift coefficient. The actuator-disk result showed a slightly lower pressure on the suction side due to the inherent time-averaging of the slipstream flowfield and therefore the lack of unsteady response of the wing. This resulted in a 3.9% increase in integrated lift, with no increase in drag.
- Almost no difference was found in the time-accurate pressure distribution on the wing at the slipstream edge between the full-blade and actuator-line model.
- The slipstream and wake agreed well in a time-average and time-accurate sense for all the propeller modeling methods. Most of the differences were those already present in the isolated propeller and wing simulations, and were mainly a result from numerical diffusion in the vortex cores.
- A clear reduction in tangential velocity was shown in the slipstream behind the wing for the propeller rotating against the rotation of the wingtip vortex compared to the rotation with the wingtip vortex in all CFD models and the experiment. With a change of flap deflection from $\delta_\mathrm{f} = -10^\circ$ to $\delta_\mathrm{f} = +10^\circ$, for all CFD models and the experiment a reduction from about 5% to about 1% was observed in the ratio of rotational to total kinetic energy.

In general, RANS CFD with a simple one-equation turbulence model (Spalart–Allmaras) is capable of modeling the interaction of the wingtip-mounted propeller in tractor configuration, provided that numerical diffusion is accounted for by a grid dependency study or prevented by local grid refinement. If the radial distribution of thrust and torque can be obtained for each azimuthal position of the blade by a lower-order method, the actuator-line model is fully capable of replacing the full-blade model. The actuator-disk model provides the ability to further reduce the cost of the simulation by removing time dependency, with a small penalty in the accuracy of the time-averaged lift distribution and flowfield. Future work will focus on a lower-order method to feed the actuator models with propeller blade loading depending on the radially and azimuthally varying inflow field.

References

[1] Loth, J. L., and Loth, F., "Induced Drag Reduction with Wing Tip Mounted Propellers," AIAA Paper 1984-2149, Aug. 1984. doi:10.2514/6.1984-2149.

[2] Miranda, L. R., and Brennan, J. E., "Aerodynamic Effects of Wingtip-Mounted Propellers and Turbines," AIAA Paper 1986-1802, June 1986. doi:10.2514/6.1986-1802.

[3] Patterson Jr, J. C., and Bartlett, G. R., "Effect of a Wing Tip-Mounted Pusher Turboprop on the Aerodynamic Characteristics of a Semi-Span Wing," AIAA Paper 1985-1286, July 1985. doi:10.2514/6.1985-1286.
[4] Janus, J. M., Chatterjee, A., and Cave, C., "Computational Analysis of a Wingtip-Mounted Pusher Turboprop," *Journal of Aircraft*, Vol. 33, No. 2, 1996, pp. 441–444. doi:10.2514/3.46959.
[5] Moore, M. D., and Fredericks, B., "Misconceptions of Electric Propulsion Aircraft and their Emergent Aviation Markets," AIAA Paper 2014-0535, Jan. 2014. doi:10.2514/6.2014-0535.
[6] Borer, N. K., Patterson, M. D., Viken, J. K., Moore, M. D., Clarke, S., Redifer, M. E., Christie, R. J., Stoll, A. M., Dubois, A., Bevirt, J., Gibson, A. R., Foster, T. J., and Osterkamp, P. G., "Design and Performance of the NASA SCEPTOR Distributed Electric Propulsion Flight Demonstrator," AIAA Paper 2016-3920, June 2016. doi:10.2514/6.2016-3920.
[7] Goldsmith, I. M., "A Study to Define the Research and Technology Requirements for Advanced Turbo/Propfan Transport Aircraft," NASA CR-166138, Feb. 1981.
[8] Kim, S.-E., and Rhee, S. H., "Efficient Engineering Prediction of Turbulent Wing Tip Vortex Flows," *Computer Modeling in Engineering & Sciences (CMES)*, Vol. 62, No. 3, 2010, pp. 291–309. doi:10.3970/cmes.2010.062.291.
[9] Bousquet, J. M., and Gardarein, P., "Improvements on Computations of High Speed Propeller Unsteady Aerodynamics," *Aerospace Science and Technology*, Vol. 7, No. 6, 2003, pp. 465–472. doi:10.1016/S1270-9638(03)00046-4.
[10] Roosenboom, E. W. M., Stürmer, A., and Schröder, A., "Advanced Experimental and Numerical Validation and Analysis of Propeller Slipstream Flows," *Journal of Aircraft*, Vol. 47, No. 1, 2010, pp. 284–291. doi:10.2514/1.45961.
[11] Gomariz-Sancha, A., Maina, M., and Peace, A. J., "Analysis of Propeller-Airframe Interaction Effects Through a Combined Numerical Simulation and Wind-Tunnel Testing Approach," AIAA Paper 2015-1026, Jan. 2015. doi:10.2514/6.2015-1026.
[12] Moens, F., and Gardarein, P., "Numerical Simulation of the Propeller/Wing Interactions for Transport Aircraft," AIAA Paper 2001-2404, June 2001. doi:10.2514/6.2001-2404.
[13] Troldborg, N., Sørensen, J. N., and Mikkelsen, R. F., "Actuator Line Modeling of Wind Turbine Wakes," Ph.D. thesis, Technical University of Denmark, 2009.
[14] Chirico, G., Szubert, D., Vigevano, L., and Barakos, G. N., "Numerical Modelling of the Aerodynamic Interference Between Helicopter and Ground Obstacles," *CEAS Aeronautical Journal*, Vol. 8, No. 4, 2017, pp. 589—611. doi:10.1007/s13272-017-0259-y.
[15] van Arnhem, N., Sinnige, T., Stokkermans, T. C. A., Eitelberg, G., and Veldhuis, L. L. M., "Aerodynamic Interaction Effects of Tip-Mounted Propellers Installed on the Horizontal Tailplane," AIAA Paper, Jan. 2018.
[16] Sinnige, T., de Vries, R., Della Corte, B., Avallone, F., Ragni, D., Eitelberg, G., and Veldhuis, L. L. M., "Unsteady Pylon Loading Caused by Propeller-Slipstream Impingement for Tip-Mounted Propellers," *Journal of Aircraft*, (in press).
[17] Sørensen, J. N., Shen, W. Z., and Munduate, X., "Analysis of Wake States by a Full-Field Actuator Disc Model," *Wind Energy*, Vol. 1, No. 2, 1998, pp. 73–88. doi:10.1002/(SICI)1099-1824(199812)1:2<73::AID-WE12>3.0.CO;2-L.
[18] ANSYS® Academic Research Release 16.0, "Help System, Fluent," ANSYS, Inc.
[19] Barth, T. J., and Jesperson, D. C., "The Design and Application of Upwind Schemes on Unstructured Meshes," AIAA Paper 1989-366, Jan. 1989. doi:10.2514/6.1989-366.
[20] Spalart, P., and Allmaras, S., "A One-Equation Turbulence Model for Aerodynamic Flows," AIAA Paper 1992-439, June 1992. doi:10.2514/6.1992-439.
[21] Dacles-Mariani, J., Zilliac, G. G., Chow, J. S., and Bradshaw, P., "Numerical/Experimental Study of a Wingtip Vortex in the Near Field," *AIAA Journal*, Vol. 33, No. 9, 1995, pp. 1561–1568. doi:10.2514/3.12826.
[22] Menter, F. R., "Two-Equation Eddy-Viscosity Turbulence Models for Engineering Applications," *AIAA Journal*, Vol. 32, No. 8, 1994, pp. 1598–1605. doi:10.2514/3.12149.
[23] Ruiz-Calavera, L. P., and Perdones-Diaz, D., "CFD Computation of In-Plane Propeller Shaft Loads," AIAA Paper 2013-3798, July 2013. doi:10.2514/6.2013-3798.
[24] Ortun, B., Boisard, R., and Gonzalez-Martino, I., "In-Plane Airloads of a Propeller with Inflow Angle: Prediction vs. Experiment," AIAA Paper 2012-2778, June 2012. doi:10.2514/6.2012-2778.
[25] Méheut, M., "Thrust and Torque Far-field Analysis of Propeller and Counter Rotating Open Rotor Configurations," AIAA Paper 2013-2803, June 2013. doi:10.2514/6.2013-2803.
[26] Falissard, F., Boisard, R., and Delattre, G., "Aeroacoustic Computation of a Contra Rotating Open Rotor Model with Test Rig Installation Effects," AIAA Paper 2012-2218, June 2012. doi:10.2514/6.2012-2218.
[27] Spalart, P. R., and Rumsey, C. L., "Effective Inflow Conditions for Turbulence Models in Aerodynamic Calculations," *AIAA Journal*, Vol. 45, No. 10, 2007, pp. 2544–2553. doi:10.2514/1.29373.
[28] Roache, P. J., "Quantification of Uncertainty in Computational Fluid Dynamics," *Annual Review of Fluid Mechanics*, Vol. 29, No. 1, 1997, pp. 123–160. doi:10.1146/annurev.fluid.29.1.123.
[29] Eça, L., and Hoekstra, M., "Discretization Uncertainty Estimation Based on a Least Squares Version of the Grid Convergence Index," *Proceedings of the Second Workshop on CFD Uncertainty Analysis*, Oct. 2006.
[30] Ekaterinaris, J. A., "High-Order Accurate, Low Numerical Diffusion Methods for Aerodynamics," *Progress in Aerospace Sciences*, Vol. 41, No. 3-4, 2005, pp. 192–300. doi:10.1016/j.paerosci.2005.03.003.
[31] Thom, A., and Duraisamy, K., "Computational Investigation of Unsteadiness in Propeller Wake–Wing Interactions," *Journal of Aircraft*, Vol. 50, No. 3, 2013, pp. 985–988. doi:10.2514/1.C031866.

This article has been cited by:

1. Pradeep Baskaran, Biagio Della Corte, Martijn van Sluis, Arvind Gangoli Rao. 2022. Aeropropulsive Performance Analysis of Axisymmetric Fuselage Bodies for Boundary-Layer Ingestion Applications. *AIAA Journal* **60**:3, 1592-1611. [Abstract] [Full Text] [PDF] [PDF Plus]
2. Pooneh Aref, Mehdi Ghoreyshi, Adam Jirasek, Jurgen Seidel. Comparison of Multi-Fidelity Prediction Methods for an Integrated Propeller . [Abstract] [PDF] [PDF Plus]
3. Rogério Rodrigues da Silva Filho, Guilherme de Souza Papini. 2021. Numerical analysis of pressure distribution in a low aspect ratio wing with distributed electric propulsion. *Journal of the Brazilian Society of Mechanical Sciences and Engineering* **43**:3. . [Crossref]
4. Pooneh Aref, Christopher Hummer, Mehdi Ghoreyshi, Adam Jirasek, Jurgen Seidel. Application of the HPCMP CREATETM-AV Kestrel to the 1st AIAA Workshop for Integrated Propeller Prediction . [Abstract] [PDF] [PDF Plus]
5. Marco Palermo, Roelof Vos. Experimental Aerodynamic Analysis of a 4.6%-Scale Flying-V Subsonic Transport . [Abstract] [PDF] [PDF Plus]
6. Michael Schollenberger, Thorsten Lutz, Ewald Krämer. Boundary Condition Based Actuator Line Model to Simulate the Aerodynamic Interactions at Wingtip Mounted Propellers 608-618. [Crossref]
7. Nando v. Arnhem, Roelof Vos, Leo L. Veldhuis. Aerodynamic Loads on an Aft-Mounted Propeller Induced by the Wing Wake . [Citation] [PDF] [PDF Plus]
8. Tomas Sinnige, Nando van Arnhem, Tom C. A. Stokkermans, Georg Eitelberg, Leo L. M. Veldhuis. 2019. Wingtip-Mounted Propellers: Aerodynamic Analysis of Interaction Effects and Comparison with Conventional Layout. *Journal of Aircraft* **56**:1, 295-312. [Abstract] [Full Text] [PDF] [PDF Plus] [Supplementary Material]
9. Nando v. Arnhem, Tomas Sinnige, Tom C. Stokkermans, Georg Eitelberg, Leo L. Veldhuis. Aerodynamic Interaction Effects of Tip-Mounted Propellers Installed on the Horizontal Tailplane . [Citation] [PDF] [PDF Plus]